Bulletin of the Seismological Society of America, Vol. 103, No. 5, pp. 2621–2644, October 2013, doi: 10.1785/0120120358

Ⓔ

Kinematic Inversion of Physically Plausible Earthquake Source Models Obtained from Dynamic Rupture Simulations

by Ali Ozgun Konca, Yoshihiro Kaneko, Nadia Lapusta, and Jean-Philippe Avouac

Abstract One approach to investigate earthquake source processes is to produce kinematic source models from inversion of seismic records and geodetic data. The setup of the inversion requires a variety of assumptions and constraints to restrict the range of possible models. Here, we evaluate to what extent physically plausible earthquake scenarios are reliably restituted in spite of these restrictions. We study which characteristics of ruptures, such as rupture velocity, slip distribution, stress drop, rise time, and slip function, can be reliably determined from the inversion of near-field seismic and geodetic data. Using spontaneous dynamic rupture simulations, we generate five earthquake scenarios, each of which has different characteristics of the source process. Then we conduct a blind test by modeling the synthetic near-source data using a standard inversion scheme that optimizes the fit to the observations while searching for solutions with minimum roughness. The inversion procedure assumes a rupture front propagating away from the hypocenter with variable rupture velocity and a simple cosine slip-time function. Our results show that, overall, slip distribution and stress drop are reasonably well determined even for input models with relatively complex histories (such as a subshear rupture transitioning to supershear speeds). Depth-averaged rupture velocities are also reasonably well resolved although their estimate progressively deteriorates away from the hypocenter. The local rise time and slip function are not well resolved, but there is some sensitivity to the rupture pulse width, which can be used to differentiate between pulse-like and crack-like ruptures. Our test for understanding the inaccuracies in Green's functions shows that random 3D perturbations of 5% standard deviation do not lead to significant degradation of the estimation of earthquake source parameters. As remedies to the current limitations, we propose smoothing slip function parameters and using more complicated inversion schemes only if data necessitates them.

Online Material: Figures showing snapshots of forward and inverse modeling of rupture, L curves, slip models, and waveform fits.

Introduction

It has become a standard practice in seismology to derive earthquake source models from the inversion of strong-motion, teleseismic, and geodetic data. For large earthquakes, the finite size of the fault needs to be taken into account. Such source models, commonly referred to as kinematic finite-fault source models, represent the slip history on the fault, which is discretized in elementary rectangular subfaults treated as one or a collection of point sources (e.g., Trifunac and Udwadia, 1974; Olson and Apsel, 1982; Hartzell and Heaton, 1983; Archuleta, 1984; Cohee and Beroza, 1994; Wald and Heaton, 1994; Cotton and Campillo, 1995). Such models provide estimates of the slip distribution, rupture velocity, and rise-time distribution (i.e., the time it takes for slip at a particular point on the fault to reach its final value).

Modern views regarding earthquake physics have been inferred, to a large extent, from the kinematic source models. Such source models revealed that earthquakes consist of successive ruptures of high-slip patches, often called asperities (Lay *et al.*, 1982). Based on the kinematic source models available at the time, Heaton (1990) showed that the rise time is much shorter than both the total source duration and the time required for the rupture to receive the healing (or stopping) phase due to the effective seismogenic width of faults, suggesting that earthquake ruptures propagate as self-healing slip pulses. Potential explanations for the short rise time on

the fault include fault heterogeneity that produces local arrest phases (Beroza and Mikumo, 1996) and strong velocity dependence of the friction law (Heaton, 1990), which can result from shear heating (Rice, 2006). It is possible, based on crack theory, to relate rupture velocity to fracture energy (Husseini *et al.*, 1975; Andrews, 1976; Husseini and Randall, 1976), and hence kinematic source models can be used to estimate fracture energy and radiation efficiency of seismic ruptures. Kinematic models can also be used to demonstrate examples of supershear seismic ruptures (e.g., Bouchon *et al.*, 2001; Konca *et al.*, 2010), and to assess fault frictional properties (Ide and Takeo, 1997). However, this can be challenging. Guaterri and Spudich (2000) and Guaterri *et al.* (2001) showed in particular that dynamic source models with different critical slip distances but same fracture energy lead to almost identical seismograms in the frequency band commonly used to derive kinematic source models. This would indicate that while fracture energy can in principle be reliably estimated, friction parameters such as the critical slip weakening distance might not be resolvable. In any case this discussion emphasizes that our ability to investigate earthquake source physics depends critically on the resolution power and reliability of finite-fault kinematic models.

The inversion techniques used to determine earthquake source models do suffer from various issues, often limiting our ability to investigate the details of earthquake source physics or leading to biased results. One such issue is the nonuniqueness of kinematic models. Monelli and Mai (2008) showed that there is generally not just one single model, but an ensemble of models that explain the data equally well. For example, inferred source models of the 1999 Izmit earthquake, for which strong-motion records, remote sensing, and geodetic data are available in addition to the teleseismic records, are strikingly different (Yagi and Kikuchi, 2000; Bouchon *et al.*, 2002; Delouis *et al.*, 2002; Sekiguchi and Iwata, 2002). The differences may be partly due to the different datasets used in those studies. It is reasonable to assume that the most reliable source model would be the one obtained from the joint inversion of all the data available in order to limit the trade-offs among the various model parameters (Konca *et al.*, 2007). However, while an extensive and diverse dataset certainly improves the resolution, there is no guarantee that the obtained source model is a good representation of the real source due to potential methodological bias (e.g., Beresnev, 2003).

The blind test of Mai *et al.* (2007) is a clear illustration of this issue. In the test, abundant near-field strong-motion synthetics were provided for a relatively simple source and known fault geometry. Yet, the slip distributions of the kinematic models obtained by different groups turned out to be widely different, and 5 out of 9 kinematic models did not perform any better than a random correlated slip model (Mai *et al.*, 2007). This problem is likely due to the many simplifying assumptions and potential methodological bias in kinematic source inversion; the fault is assumed to be planar or to consist of a limited number of planes gridded into small rectangular subfaults; slip is assumed to be uniform within each subfault; the rupture starts at a predetermined hypocenter; a single rupture front is usually assumed, so that each point on the fault starts slipping at a time determined by the rupture velocity; the time evolution of slip during the rise time (hereafter called the rise-time function) is generally imposed to be multiple time window triangular functions for fixed rupture-velocity models (Hartzell and Heaton, 1983), or some simple analytical functions with typically 1 or 2 adjustable parameters when rupture velocity is allowed to vary (Archuleta, 1984; Cohee and Beroza, 1994; Cotton and Campillo, 1995). In addition to these assumptions, regularization is needed because the inversion is generally ill-posed due to the large number of model parameters. Most commonly used regularization is achieved by constraining the source model to be as smooth as possible in terms of the time evolution of the rupture and of the slip distribution. A common practice relies on the assumption of a constant rupture velocity, or a velocity that varies within a bounded range, and on imposing a smooth slip distribution by penalizing its Laplacian (Harris and Segall, 1987) or using correlation lengths (Hernandez *et al.*, 1999). These assumptions determine the space of source models within which the best-fitting model is sought during the inversion procedure. However, there is no guarantee that these assumptions are applicable to real earthquake sources. For example, the parameterization described above penalizes noncontiguous fault patches to be sliding at the same time, while this kind of behavior occurs in dynamic models and hence may occur during earthquakes.

In this study, we test the ability of a commonly used nonlinear inversion procedure to retrieve the main characteristics of physically plausible earthquake sources, such as a slip distribution, rupture velocity, and rise times. In particular, we assess how well pulse-like nature of earthquake ruptures, distributions of seismic asperities, or acceleration of rupture velocity to supershear speeds, can be retrieved from inversions of synthetic seismic and geodetic data. To produce physically plausible sources with different rise times, spatiotemporal slip distributions, rupture velocity etc., we use simulations of spontaneous dynamic rupture (Kaneko *et al.*, 2008). We then apply to the synthetic data the inversion method of Ji *et al.* (2002), which has been commonly used in finite-fault models of earthquakes using geodetic, near-source, and teleseismic data (Ji *et al.*, 2001, 2003, 2004; Shao and Ji, 2011). Hereafter we describe the forward scenarios and the inverted source models, and evaluate what information is reliably retrieved and what information is biased. We finally discuss possible methodological improvements to produce more reliable earthquake source models.

Methodology

Strategy of the Study

We have adopted a blind test strategy, with the team in charge of the kinematic inversion not knowing the

characteristics (moment, rupture velocity, slip distribution, and rake angles) of the input dynamic models.

As the first step, the dynamic modeling team has designed different scenarios, created forward models using a dynamic rupture simulation code, and generated the corresponding seismograms and static displacements at the locations of a hypothetical array of near-field stations. Four different scenarios have been produced, with different characteristics of the source process: crack-like versus pulse-like rupture, single versus multiple asperities, or subshear versus supershear rupture. In all the scenarios, the fault is planar, vertical, and strike slip. In the first three scenarios, we consider a homogeneous elastic half-space with the *P*-wave speed of 6.0 km/s and the *S*-wave speed of 3.46 km/s. A layered half-space model and a model with random velocity variations are used for the fourth and fifth scenario, respectively. All the source scenarios considered in our study are still relatively simple (e.g., there are no fractal variations in source properties and the fault is planar). While complex, presumably more realistic, rupture scenarios can be constructed with a stochastic distribution of prestress (e.g., Lavallee *et al.*, 2006), we choose to generate relatively simple scenarios to address certain issues such as crack versus pulse mode of slip, resolving complex slip distribution, multiple rupture fronts, super-shear rupture and uncertainties of the velocity structure. Analyzing more complex scenarios, including fault nonplanarity, is left for future work.

As the second step, kinematic finite-source models have been determined from the inversion of these synthetic data. The information available for kinematic modeling includes the fault strike and dip, the hypocenter location, the bulk velocity model, and the three-component waveforms and static displacements (i.e., the values of displacement in three components at the end of each simulation) at 36 stations all located on the earth's surface. The seismograms are band-pass filtered between 0.75 and 50 s, to mimic the bandwidth limitation of accelerometric measurements at low frequencies and to limit the analysis to the frequencies that are generally used in earthquake studies. (Higher frequencies are more attenuated and more affected by path effects, which can distort resolution of the source.) This approach mimics a dataset consisting of near-field accelerometric measurements and Global Positioning System (GPS) measurements. The static displacements at all the stations are used in all the inversions. Note that ground deformation measured from Interferometric Synthetic Aperture Radar (InSAR) or from correlation of optical or Synthetic Aperture Radar (SAR) amplitude images can provide an even denser coverage in real earthquakes. For scenarios 1–3, waveforms recorded at nine stations and the static displacements at all the stations are used. For scenario 4, the inversion of nine seismic data with the given T-shaped distribution of stations that are used for the first three scenarios did not converge to an acceptable fit to the data, and the inversion here uses waveforms from 18 stations nearest to the fault plane while still following all the other assumptions.

This study is different from a resolution test, which compares forward and inverse models all parameterized in the same way. The dynamic models do not generally fulfill the constraints on the rupture velocity, rise time, and rise-time function imposed in the kinematic source models. Note also that the sensitivity of our inversion procedure to data noise is not addressed in this study. We do, however, consider the effect of heterogeneities or imprecise knowledge of the subsurface elastic structure, as it has been shown that improperly accounting for such heterogeneities can bias finite-fault source models (Graves and Wald, 2001; Wald and Graves, 2001).

Dynamic Forward Modeling

We produce five dynamic rupture scenarios on a vertical strike-slip fault embedded into either a homogeneous or layered elastic half-space except scenario 5, in which 3D perturbations are added to the half-space model. The fault is governed by rate-and-state friction with the aging form of state variable evolution. For time-independent effective normal stress σ, the shear strength τ is expressed as

$$\tau = \sigma[f_0 + a\ln(V/V_0) + b\ln(V_0\theta/L)]\, d\theta/dt = 1 - V\theta/L, \tag{1}$$

in which a and b are the rate-and-state constitutive parameters, V is slip rate, f_0 is the reference friction coefficient corresponding to the reference slip rate V_0, θ is a state variable, and L is the characteristic slip for state evolution (Dieterich, 1978, 1979; Ruina, 1983). The actual fault resistance to sliding in our model is given by this formulation regularized at zero slip velocity (e.g., Rice and Ben-Zion, 1996; Lapusta *et al.*, 2000). The response of the constitutive laws (equation 1), when extrapolated to coseismic slip rates, becomes qualitatively similar to the one given by linear slip-weakening friction (Cocco and Bizzarri, 2002) commonly used in dynamic rupture models (Day *et al.*, 2005).

We solve the elastodynamic equations coupled with the friction law (equation 1) using a spectral element method (Ampuero, 2002; Kaneko *et al.*, 2008). On the fault, the strike component of slip and shear traction are solved for numerically; for simplicity, we impose a fixed rake in all the source scenarios. Absorbing conditions are used for all boundaries of the model domain except the free surface, to mimic a semi-infinite elastic half-space. The dynamic rupture code we use has been validated through the Southern California Earthquake Center Dynamic Rupture Code Verification Exercise (Harris *et al.*, 2009) and has been used in studies of dynamic rupture (Kaneko *et al.*, 2008; Kaneko and Lapusta, 2010; Kaneko and Fialko, 2011).

The setup is designed to produce a crack-like rupture of a simple rectangular patch in scenario 1, a pulse-like rupture of a simple rectangular patch in scenario 2, and a pulse-like rupture of two asperities in scenario 3. Scenario 4 involves transition to supershear rupture, with two rupture fronts for a period of time. In scenario 5, the forward models are computed assuming a randomly generated heterogeneous elastic medium and we invert the output of this model with

Green's functions computed for a 1D elastic medium. This scenario allows testing the effects of using inadequate Green's functions in the inversion. In our dynamic rupture simulations, the rise-time scales with the width of the seismogenic zone. In scenario 1, the width of the seismogenic zone is chosen to be wider than in the other scenarios, resulting in longer rise times and more crack-like rupture. In scenario 4, we prescribed variable depth-dependent prestress in order to produce supershear rupture. Scenario 5 considers the same pulse-like rupture of two asperities as in scenario 3 but placed in a heterogeneous elastic structure.

For all the scenarios, the effective normal stress increases with depth due to the difference of overburden minus hydrostatic pore pressure ($\sigma = \min[1.0 + 16.2\ z,\ 80.0]$ MPa, in which z is in kilometers) and becomes constant (80 MPa) at depths larger than 4.9 km. The distributions of shear prestress and other fault parameters differ in each scenario and are described in the subsequent section. The medium is initially moving on the two sides of the fault with equal and opposite horizontal particle velocities of $V_{\text{in}}/2 = 5 \times 10^{-13}$ m/s, values much smaller than typical plate loading rates of 10^{-10} to 10^{-9} m/s. Starting at time $t = 0$, dynamic rupture is initiated by imposing a rapid but smooth time-dependent variation of the horizontal shear traction in a circular patch. The details of the nucleation procedure are described in Kaneko *et al.* (2008).

The model domain is 200 km (along strike)× 200 km (perpendicular to strike) × 72 km (along dip). It is discretized with a uniform mesh with the average node spacing of 0.1 km. The element size is small enough to sufficiently resolve the dynamic rupture on the fault. The time step is 0.005 s. Our synthetic seismograms are accurate for periods longer than 0.1–0.2 s.

Kinematic Inversion Method

The synthetic data are inverted for kinematic finite-fault source models using the method of Ji *et al.* (2002). This commonly used kinematic inversion code allows for the joint inversion of seismological records, both teleseismic and near field, as well as static displacements measured from both GPS and remote sensing (e.g., Ji *et al.*, 2003, 2004; Konca *et al.*, 2008, 2010; Sladen *et al.*, 2010; Shao and Ji, 2011). This method does not differ fundamentally from the other methods used for the joint inversion of seismological and geodetic data (e.g., Delouis *et al.*, 2002; Liu and Archuleta, 2004). It employs a simulated annealing method, searching a bounded parameter space starting from a random model to converge to the best-fitting model. The joint inversions require fitting the seismograms and static displacement data simultaneously. The seismograms are calculated from

$$u(t) = \sum_{j=1}^{n} \sum_{k=1}^{m} D_{jk} \times Y_{jk}(x, t - d_{jk}/V_{jk}) \times \dot{S}_{jk}(t), \quad (2)$$

in which j and k are indexes of summation along strike and dip, respectively, Y_{jk} are the subfault Green's functions computed according to the assumed seismic-velocity model (homogeneous or layered half-space), D_{jk} are slips on subfaults, V_{jk} are the rupture velocities between the hypocenter and subfaults, and d_{jk} are the distances of the subfaults from the hypocenter. The subfault size is set to 1.8 km along strike and 1.5 km along dip so that details of the rupture resolvable given the station distribution are resolved, while large enough to avoid a too long computation time. The kinematic Green's functions are generated by a frequency–wavenumber algorithm (Zhu and Rivera, 2001).

The slip history at each point on the fault is given by $D \times \dot{S}_{jk}(t)$, in which $\dot{S}_{jk}(t)$ is the rise-time (or the slip-rate) function that specifies how a point on the fault slips in time. The integral f is normalized to 1 so that D is the cumulative (or static) slip. The rise-time function is represented by two modified cosine functions, for the monotonic increase and decrease of the slip velocity at each point, t_s and t_e (Ji *et al.*, 2003):

$$\dot{S}(t) = \begin{cases} \frac{1}{t_s + t_e}\left[1 - \cos\frac{\pi t}{t_s}\right], & 0 < t < t_s \\ \frac{1}{t_s + t_e}\left[1 + \cos\frac{\pi(t - t_s)}{t_e}\right], & t_s < t < t_s + t_e \\ 0, & t > t_s + t_e \end{cases}. \quad (3)$$

In this formulation, the slip-rate function is asymmetrical if t_s and t_e are different. The reason for the two-parameter rise-time function rather than a symmetric function is that, based on dynamic rupture studies, the slip velocity is expected to have a Kostrov-type shape with slip velocity increasing abruptly at the onset of rupture and decreasing slowly following the peak particle velocity (Tinti *et al.*, 2005). To limit the number of parameters to be inverted for, the sliding rate function is often assumed to be symmetrical. That case, in which $t_s = t_e$, is referred to in the following as the one-parameter slip-rate function.

These seismograms are transformed to the wavelet domain to characterize their time-variable frequency content in a compact form using only the wavelets covering periods of 0.75–50 s.

The misfit between the observed and predicted waveforms is quantified in the wavelet domain using the sum of L1 and L2 norms (Ji *et al.*, 2002):

$$e_{wf} = \sum_{j=j_{\min}}^{j=jc} w_j \times \left(\frac{1}{k_j} \sum_{k}^{k_j} |o_{j,k} - y_{j,k}| + \sqrt{\frac{1}{k_j} \sum (o_{j,k} - y_{j,k})^2} \right), \quad (4)$$

in which $o_{j,k}$ and $y_{j,k}$ are the wavelet coefficients of the observed and synthetic seismogram for station k and wavelet index j, and w_j is the weight of each wavelet channel. In this study, we keep the weight on each wavelet channel w_j the same.

The static displacement Green's functions are calculated with the method of Xie and Yao (1989). The misfit between

Table 1
Bounds of the Range of Parameters Used for Kinematic Inversion for Each Scenario

	Rupture Velocity (km/s)	Rise Time (s)	Slip (m)	Rake(°)
Scenario 1	2–4	0.4–4	0–6	160–200
Scenario 2	2–4	0.4–4	0–6	160–200
Scenario 3	2–4	0.4–4	0–6	160–200
Scenario 4	2–6	0.4–6	0–10	160–200
Scenario 5	2–4	0.4–4	0–6	160–200

the observed and predicted static displacements is quantified from the root mean square of the residuals:

$$e_{\text{stat}} = \frac{1}{n}\sum_{i=1}^{i=n}(\text{pred}^i - \text{obs}^i)^2, \quad (5)$$

in which n is the number of geodetic data, obs^i is the observed displacements at station i, and pred^i is the predicted displacement at station i.

In addition, we regularize the inversion by minimizing the Laplacian of the slip distribution. The objective function which is minimized in the inversion is then written as

$$O = e_{wf} + w_{\text{stat}} e_{\text{stat}} + w_s \Delta_s + w_T \Delta_T, \quad (6)$$

in which w_{stat} is the weight put on the misfit to the static displacement data, w_s is the weight put on the Laplacian of the slip distribution Δ, and w_T is the weight put on the Laplacian of the rupture time Δ_T (the differential time at which the rupture front reaches each node with respect to a constant rupture velocity). w_{stat} is chosen so that the weight of the geodetic and seismic data is the same in the inversion. The weight on the rupture time smoothing Δ_T is calibrated to be large enough to avoid noncausal slip.

All inversions start with a random initial model. A new initial model is generated at the first iteration in each inversion. The weight of the misfit to the static data is then chosen so that the misfits to the waveforms and to the static displacements for the best-fitting model have equal importance in the objective function ($e_{wf} = W_{\text{stat}} \times e_{\text{stat}}$). The weight put on the Laplacian of the slip distribution is chosen based on the L-curve which shows how the misfit varies depending on the weighting. As the parameter space is searched, the objective function is minimized using a heat bath algorithm. The number of iterations is chosen large enough to ensure convergence toward a stable solution. In the heat bath algorithm, the number of iterations primarily depends on the initial temperature, and the cooling rate. In practice we set the number of iterations to 800 and check that the algorithm has indeed converged. The ranges of the model parameters (rupture velocity, rise-time, and slip) explored with the simulated annealing algorithm are given in Table 1.

Results

We describe here the results obtained from the inversion of the five scenario earthquakes. We investigate the performance of the kinematic inversion in retrieving the main characteristics of those ruptures. For each case, we obtain the slip distributions derived from the static displacement only, the kinematic source model derived from the waveforms only, and the kinematic source models derived from the joint inversion of the static displacements and of the waveforms. Two joint inversions are produced, assuming a symmetrical slip-rate function (a one-parameter rise-time function) and asymmetrical slip-rate function (two-parameter rise-time function; Fig. 1). Table 2 shows the moment magnitude, average slip, peak slip, rupture area, and stress drop of the forward dynamic models and the inverted source models for all scenarios. We also show snapshots of the distribution of sliding rate on the fault every 2 s. This allows visualizing the evolution of the rupture front.

Scenario 1: Crack-Like Rupture of a Rectangular Patch

Scenario 1 is designed as a rupture of a 12 km by 40 km rectangular velocity-weakening patch surrounded by a velocity-strengthening region. The model setup and resulting slip model with rupture time contours are shown in Figure 1a. The rupture initiates at the nucleation patch and then spontaneously propagates until it encounters the velocity-strengthening regions at the 15 km depth and at lateral distances of −10 and 30 km, where the slip gradually terminates (Fig. 1). The rupture is bilateral during the first 4 s, and becomes unilateral after that. The resulting synthetic earthquake is a crack-like M_{w} 6.99 event with the peak slip of 3.6 m and the average stress drop of 2.4 MPa.

In Figure 1b, we show the models obtained from the inversion of the geodetic data only, of the seismic data only, and of all the data. All models capture the basic characteristics of slip distribution. The joint inversion tends to stabilize the rake variations apparent in the seismic only and geodetic only models. The time contours of the rupture fronts (Fig. 1b) fluctuate more than those of the input model (Fig. 1a). Figure 2a shows the misfits to the geodetic and seismic data as a function of the model roughness. As expected, the fit to the data increases when the source becomes rougher. The corresponding models (assuming a two-parameter rise-time function) are shown in Figure 2b. This so-called L-curve is used to choose the preferred model (circled in red), which corresponds to the point on Figure 2a at which the misfit starts to increase significantly while the model roughness decreases only slightly. The choice of the preferred model is somewhat subjective, but even if a slightly smoother or rougher model were chosen, it would still reproduce the input model similar to what is shown in Figure 1.

The fit to the static displacements obtained from the joint inversion with the two-parameter rise-time function is shown

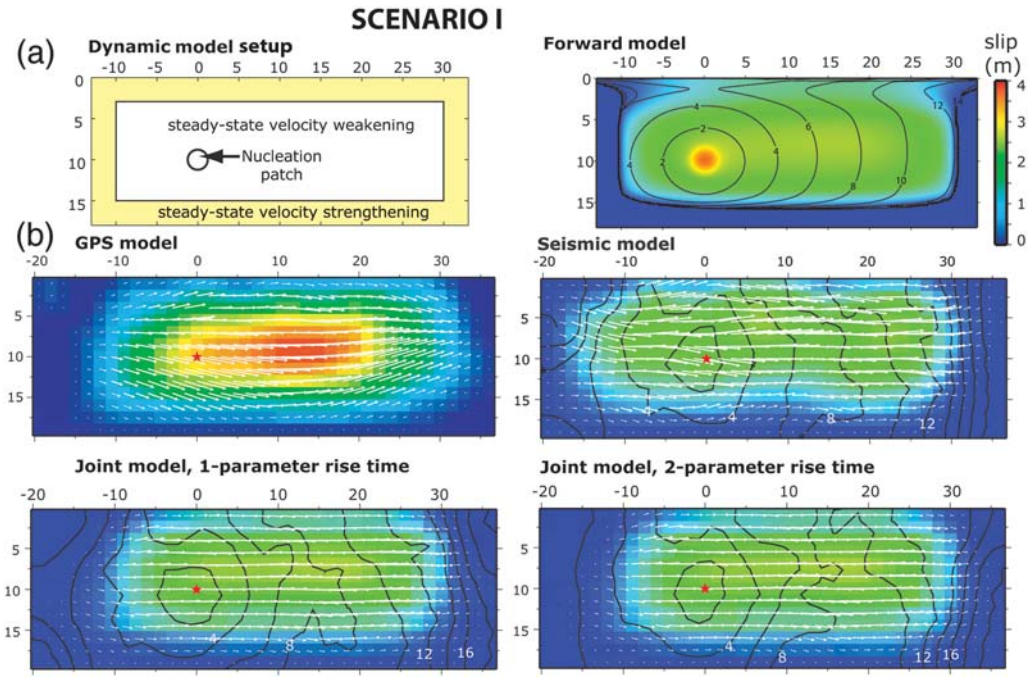

Figure 1. (a) The setup of scenario 1 for the dynamic rupture simulation (left) and resulting slip distribution with 2 s rupture time contours (right). (b) The slip distributions for the geodetic, seismic, and two-joint inversions. Rupture time contours are shown for the kinematic inversions. Hypocenter is represented by a red star.

in Figure 3a. The fits to the waveforms obtained from the joint inversion with both the one- and the two-parameter rise-time function are shown in Figure 3b. The inverted source models with one- and two-parameter rise-time function fit the static displacements and the waveforms very well. The two-parameter rise-time model yields a somewhat better fit to the waveforms than the one-parameter rise-time model (Table 2; Fig. 3b), as expected, given the larger number of

Table 2

Comparison of Seismic and Geodetic Error, Moment Magnitude, Peak and Average Slip and Stress Drop for Input and Inverted Models

		Variance Reduction* (%)	Geodetic rms	M_w	Average Slip† (m)	Peak Slip (m)	Rupture Area‡, A (km^2)	Fault Width‡, w (km)	Stress Drop§(MPa)
Scenario 1	Input	—	—	6.99	1.74	3.58	607	15	2.40
	two-parameter rise time	84.4	0.052	6.98	1.67	2.56	600	15	2.34
	one-parameter rise time	82.5	0.049	6.94	1.68	2.53	600	15	2.04
Scenario 2	Input	—	—	6.88	1.41	3.12	522	9.3	3.07
	two-parameter rise time	80.6	0.093	6.84	1.74	3.03	660	11	1.79
	one-parameter rise time	77.3	0.096	6.88	1.74	2.94	660	11	2.06
Scenario3	Input	—	—	6.91	1.53	2.86	533	9.6	3.24
	two-parameter rise time	86.6	0.056	6.88	1.10	2.71	580	10	2.57
	one-parameter rise time	83.6	0.066	6.88	1.11	2.71	580	10	2.57
Scenario 4	Input	—	—	7.37	4.76	7.34	917	16	5.53
	two-parameter rise time	84.5	4.89	7.31	4.00	8.18	870	15	5.05
	one-parameter rise time	81.8	4.87	7.36	3.93	8.04	870	15	6.00
Scenario 5	Input	—	—	6.98	1.70	3.32	569	10	3.65
	two-parameter rise time	68.8	0.084	6.94	1.43	3.48	656	11	2.96
	one-parameter rise time	68.2	0.084	6.95	1.37	3.17	694	12	2.59

*Variance reduction is calculated by $V_a = 100 - 100 \times (\int (d(t) - s(t))^2 dt)/(\int (d(t))^2 dt)$.

†The average slip is calculated in three steps: computing the average of slip over the entire fault, finding (1.8×1.5 km) subfaults that slipped 30% or more of the average value, and computing the average of slip over these subfaults. The rupture area A is defined as the sum of the areas of these subfaults.

‡The effective width is calculated by $w = A/l$, in which length l is the maximum extent of the rupture area along the fault-strike direction.

§To compute the average stress drop, we use an analytical solution for a rectangular fault of length l and width $w (l \gg w)$ (Knopoff, 1958): $\Delta\sigma = (2/\pi)M_0/(Aw)$.

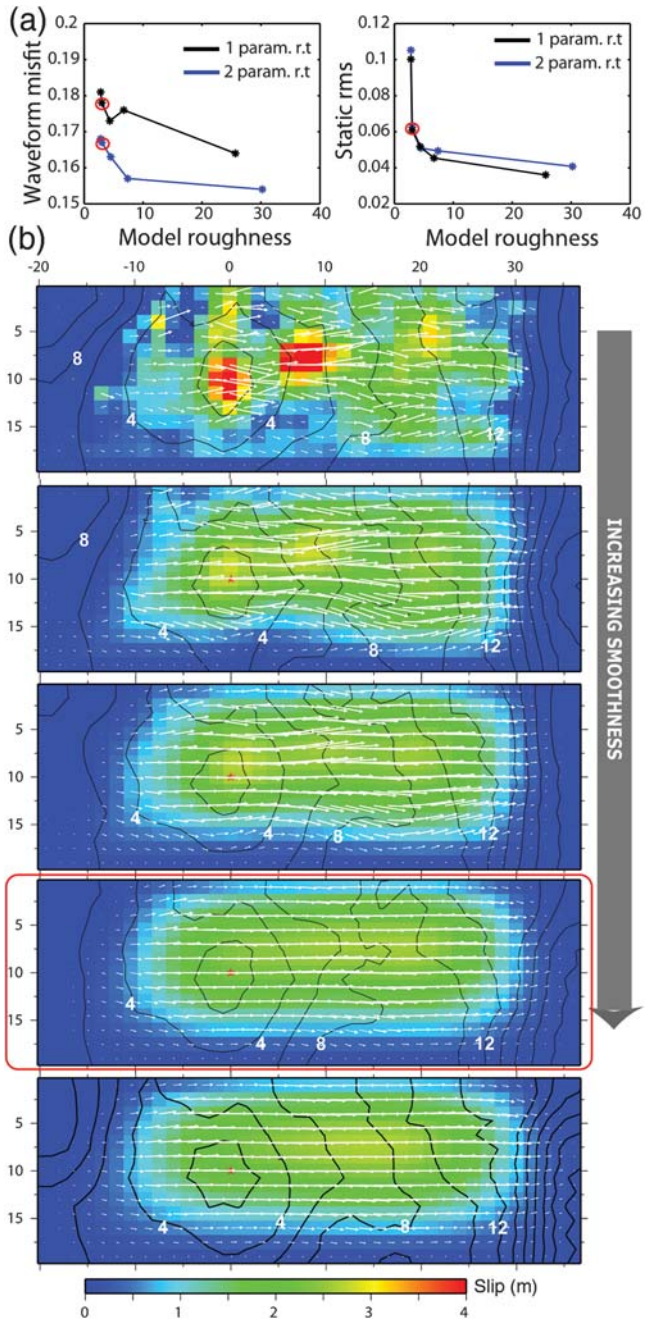

Figure 2. (a) The model roughness versus misfit curves (L-curves) for the geodetic and seismic data for scenario 1. The selected best-fit model is shown with a red circle. (b) The slip distributions for the two-parameter rise-time joint models with increasing model smoothness from top to bottom. The selected model is shown in a red rectangle.

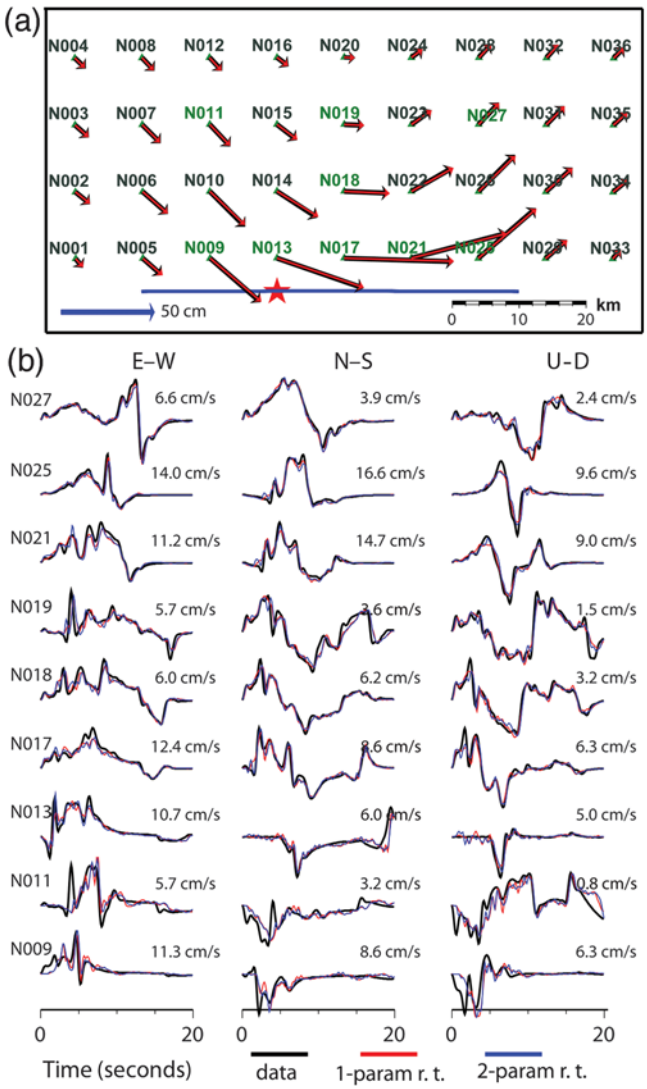

Figure 3. (a) Fits to the geodetic data for the best-fit joint model with two-parameter rise time for scenario 1. Data is in black and fits are in red. The station names are to the top left of the GPS data points. The name of the stations that are also used for seismic data are shown in green. The blue line shows the surface expression of the fault and red star represents the epicenter location. (b) Fits to the seismic data at nine stations for one-parameter (red) and two-parameter (blue) rise-time joint inversions.

adjustable parameters. The rupture extent, slip distribution, and moment magnitude of the input model are retrieved quite successfully in all the inversions (Table 2).

The input model has higher slip velocities at the rupture tip followed by a lower slip-rate tail, reflecting the crack-like nature of that rupture. This feature is not well retrieved in the inverted source models that are designed to produce pulse-like rupture (through the cosine-shaped rise-time function), although the inferred pulse is wider than the ones in some subsequent scenarios, as discussed later. The rise times tend to be close to the upper value allowed in the inversion (4 s) and are a large fraction of the total duration (12 s) (Fig. 4; Table 1). Because this scenario involves a crack-like rupture, in which slip at any point stops only after the rupture has stopped, longer rise times are expected. A test in which the upper bound on rise time is increased to 10 s gives very similar results (Ⓔ Fig. S1, available in the electronic supplement to this article). The snapshots of the slip velocity show that the kinematic models capture the location of the rupture front and the width of the actively slipping areas reasonably well, although the rupture fronts are not as sharp as those of the

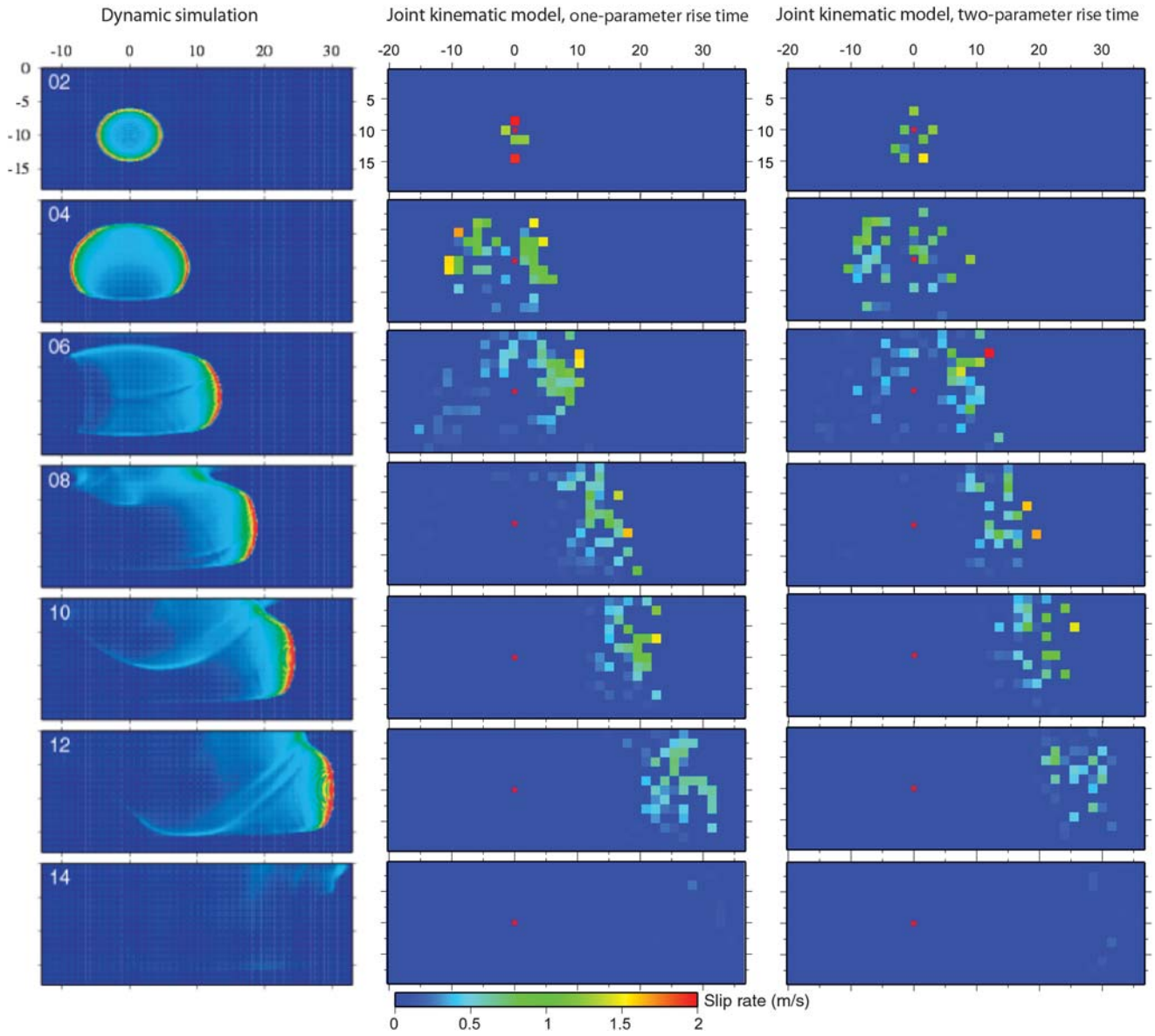

Figure 4. Snapshots of slip rate on the fault every 2 s for scenario 1 for the input model (left), joint model with one-parameter rise time (center) and joint model with two-parameter rise time (right). The velocities are saturated at 2 m/s.

input model (Fig. 4). The blur of the rupture front in the inversion is due to rapid variations of the rise time in the neighboring subfaults, because the rise times are not smoothed in the current inversion scheme. The variations in rupture velocity add to the blurriness of the pulses. The peak slip rate (2 m/s) is underestimated compared to 6 m/s in the input dynamic model. These high-slip rates are not resolvable because the stations are at the surface and the bandwidth of the waveforms for the inversion is limited (see Discussion for more details).

Nonetheless, the key features and quantitative characteristics of the rupture propagation are retrieved reasonably well from the inversion (Figs. 1 and 4; Table 2). We see that the rupture is bilateral during the first 4 s, and becomes unilateral after that (Fig. 4). The propagation of the rupture front is also well reproduced in the areas of high slip.

Scenario 2: Pulse-Like Rupture of a Rectangular Patch

Scenario 2 is a rupture of a narrower and longer, 55 km by 7.5 km, rectangular velocity-weakening patch, designed to produce pulse-like rupture due to the patch geometry. The model setup and resulting slip model with rupture time contours are shown in Figure 5a. The rupture is essentially unilateral. The rise times are shorter (2–3 s) than those in scenario 1 because they are controlled by the narrower rupture width, and small compared to the source duration (18 s),

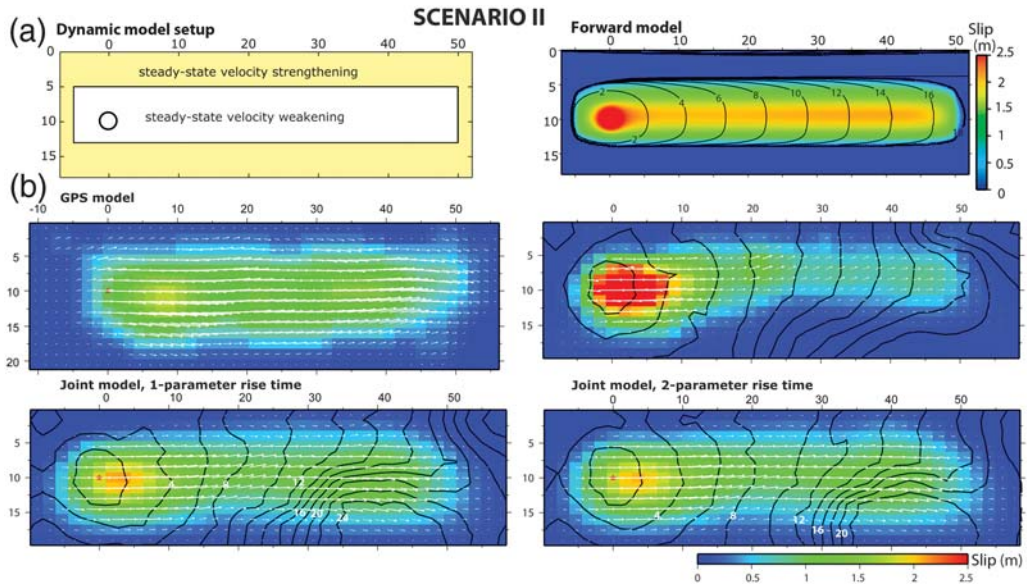

Figure 5. (a) The setup of scenario 2 for the dynamic rupture simulation (left) and resulting slip distribution with 2 s rupture time contours (right). (b) The slip distributions for the geodetic, seismic, and two-joint inversions. Rupture time contours are shown for the kinematic inversions. Hypocenter is represented by a red star.

which is controlled by rupture length. Because of the narrow width of the velocity-weakening patch, stopping phases propagate from the top and bottom of the seismogenic zone, leading to a pulse-like rupture. The resulting synthetic earthquake is an M_w 6.88 event with the peak slip of 3.1 m and the average stress drop of 3.07 MPa (Table 2).

The choice of the best-fitting smooth model (Fig. 5) is clear based on the L-curves showing the fit to the static displacements or to the waveforms as a function of the model roughness (Fig. 6a). Figure 6b shows the associated models with increasing roughness. Although the rougher models better resolve the tapering off of slip at the edges of the rupture, they lead to complex slip distributions that are not present in the input model. The choice of the preferred model based on the L-curves offers a good compromise, although the slip distribution is somewhat smoother in the geodetic model than in the input model (Fig. 5b). When the waveforms are taken into account, the short-wavelength features of the slip distribution are better retrieved (Fig. 5b, joint models). The narrow width of the rupture is better estimated with the seismic model than with the geodetic model.

The fit to the static displacements and to the waveforms obtained from the joint inversion is shown in Figure 7. The quality of the fit to both datasets is satisfactory (with at least 80% variance reduction; Table 2).

The snapshots of the slip velocity (Fig. 8) show that the inverted source models reproduce the pulse-like nature of the propagation of the rupture front reasonably well. The comparison of pulse widths of scenario 1 (Fig. 4) and scenario 2 (Fig. 8) clearly shows that the kinematic inversion has some resolution of the width of the actively slipping zone. As in scenario 1, the width of the slipping zone and its timing are well resolved, but the peak slip rate of the dynamic model (9 m/s) is smoothed out and the rupture front is more rounded in the inverted sources, as discussed in more detailed in the Discussion section.

Scenario 3: Pulse-Like Rupture of Successive Asperities

Scenario 3 is designed to yield a more complex slip distribution than scenarios 1 and 2. This is achieved by modifying the geometry of the velocity-weakening zone. As shown in Figure 9a, we consider a sinusoidal geometry for both the top and bottom edges of that zone. The resulting earthquake is an M_w 6.91 event that propagates unilaterally and ruptures two main asperities. The slip peaks to 2.9 m in those two high-slip areas for which the velocity-weakening patch is wider. The rise times vary laterally because, at any position on the fault, they are influenced by the local width of the velocity-weakening zone.

Scenario 3 is a good example for illustrating the selection process of the best-fitting model based on the L-curves. The misfits to the static displacements and to the waveforms (L-curves), and the associated slip distributions for the joint inversion with two-parameter rise time, are shown in Figure 10a and 10b, respectively. As the models get rougher, finer-scale features show up that better reveal details of the rupture initiation and the asperities. But the rougher models also show some short-wavelength artifacts in slip and rake that are not present in the input model. The roughest models do not capture the overall shapes of the asperities at all, although they do fit better the displacement and waveform data. As the models get smoother, they look more like the input model, but, at some point, the details of the asperity distribution are lost. Hence smoothing up to the point at

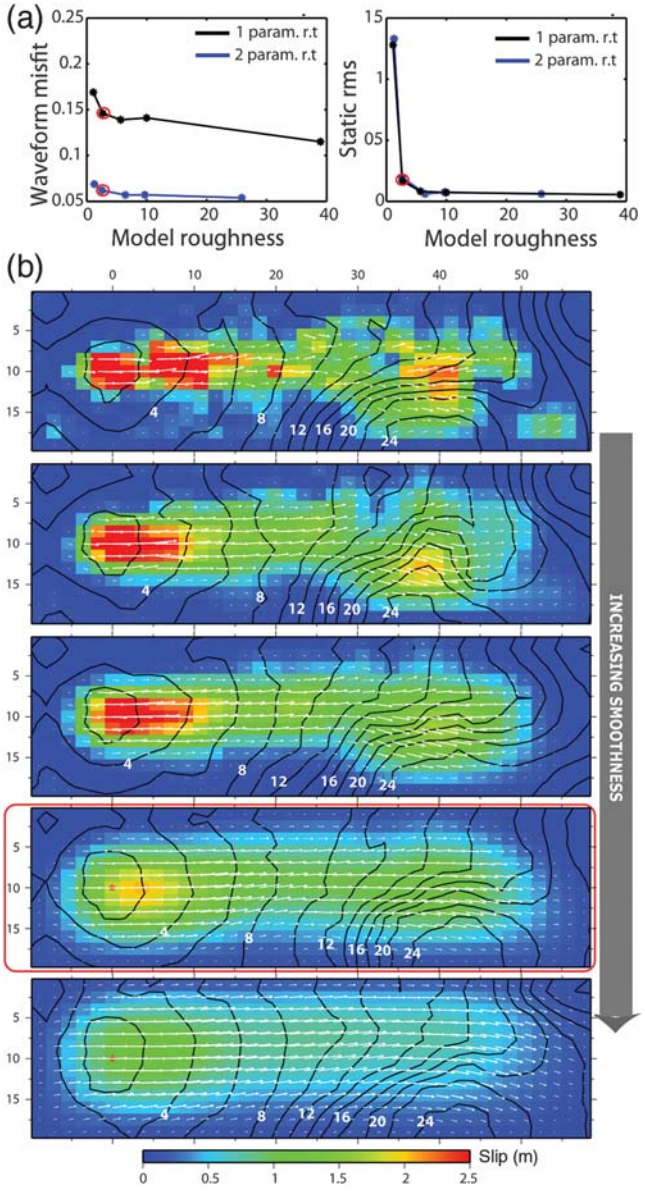

Figure 6. (a) The model roughness versus misfit curves (L-curves) for the geodetic and seismic data for scenario 2. The selected best-fit model is shown with a red circle. (b) The slip distributions for the two-parameter rise-time joint models with increasing model smoothness from top to bottom. The selected model is shown in a red rectangle.

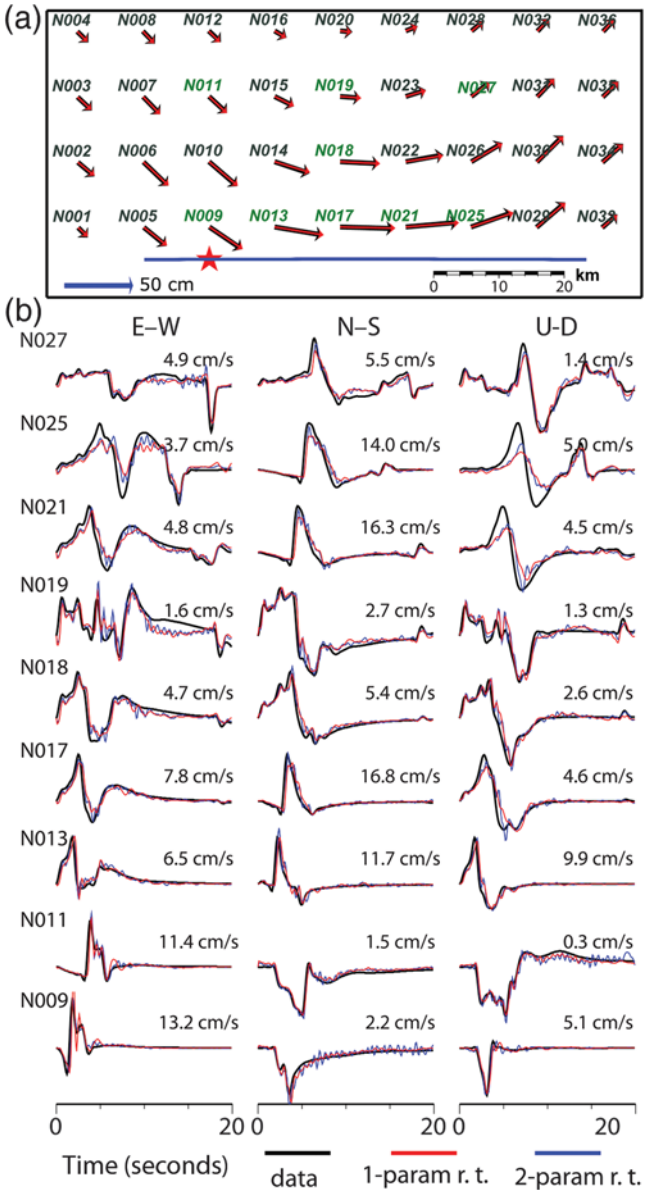

Figure 7. (a) Fits to the geodetic data for the best-fit joint model with two-parameter rise time for scenario 2. Data is in black and fits are in red. The station names are to the top left of the GPS data points. The name of the stations that are also used for seismic data are shown in green. The blue line shows the surface expression of the fault and red star represents the epicenter location. (b) Fits to the seismic data at nine stations for one-parameter (red) and two-parameter (blue) rise-time joint inversions.

which the misfit starts increasing significantly is necessary but smaller-scale features can be lost.

Figure 11 shows the fits to the static displacements and to the waveforms for the two-parameter rise-time joint inversion. The fits to the GPS and strong-motion data are very good for both joint models (Table 2).

As for scenarios 1 and 2, the slip distribution for scenario 3 is well reproduced (Fig. 9b) although the short wavelengths of the slip distribution are somewhat smoothed out. As a result, the rupture extent determined from the inversions is broadened along the dip, especially in the geodetic model. On the other hand, the GPS data helps resolve the shapes of the asperities, as they are less accurate for the seismic only model. In this example, as in the previous ones, the joint models capture many of the properties of the slip distribution.

Figure 12 shows the slip-velocity snapshots of the input model and 2 joint models (saturated at 2 m/s on the plot). Again, the rupture timing and the variations in the size of the actively slipping area are tracked by both of the one-parameter and two-parameter rise-time joint models.

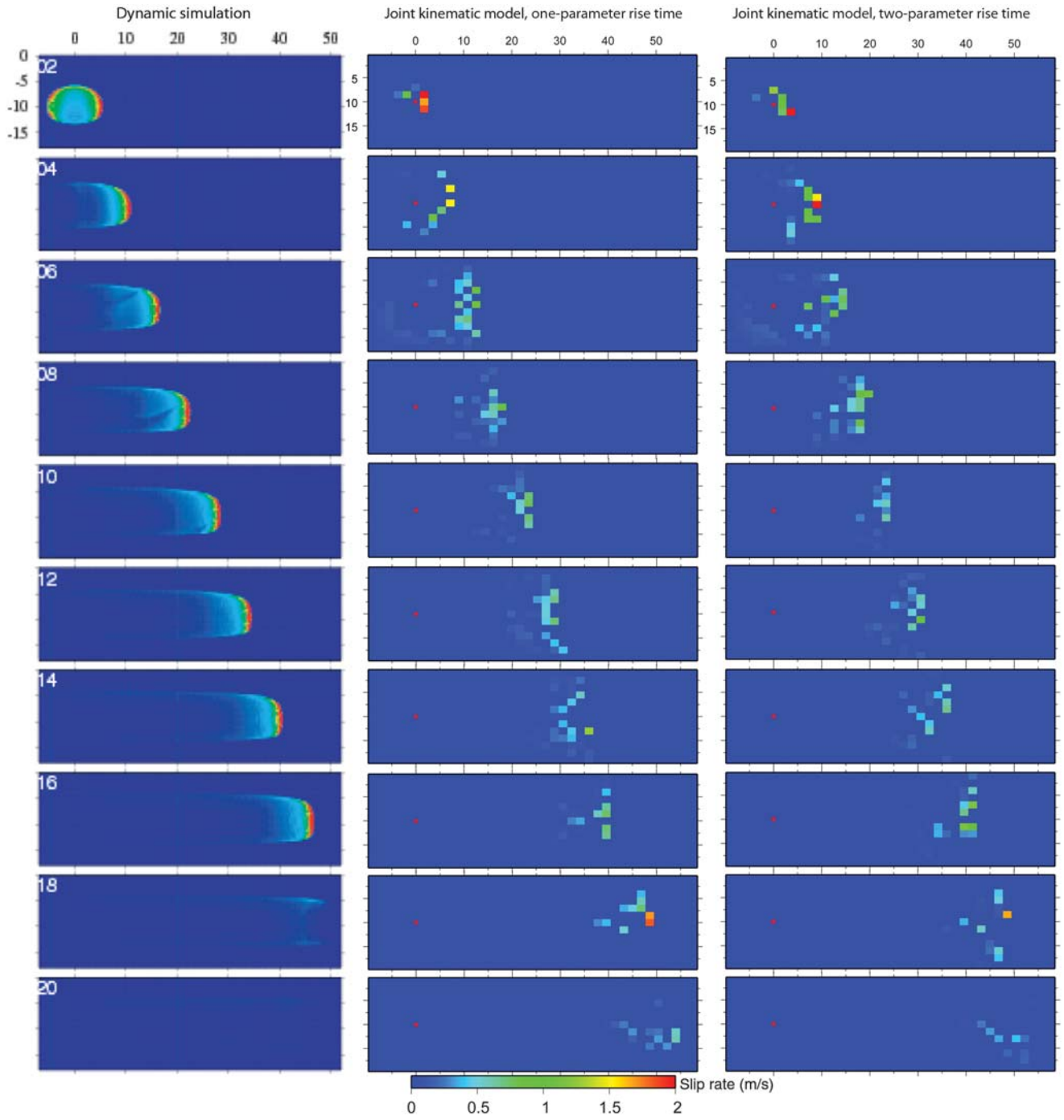

Figure 8. Snapshots of slip rate on the fault every 2 s for scenario 2 for the input model (left), joint model with one-parameter rise time (center) and joint model with two-parameter rise time (right). The velocities are saturated at 2 m/s.

For this scenario, we also compare the input and inverted slip history of two selected points on the fault (Figure 13). The input model shows higher slip velocity at the rupture front that is trailed by a zone of lower-slip velocity (Figure 13), as typical for dynamic rupture models. For the kinematic inversions, the slip rate at the rupture front is not as high as that in the input model, as mentioned above for the first two scenarios.

Scenario 4: Supershear Rupture with Multiple Rupture Fronts in Layered Bulk

Scenario 4 is meant to represent a more complex earthquake. The velocity-weakening zone is a 55 km by 7.5 km rectangular patch, as in scenario 2. However, a three-layer velocity structure is used instead of a uniform half-space, along with variable depth-dependent initial shear stress

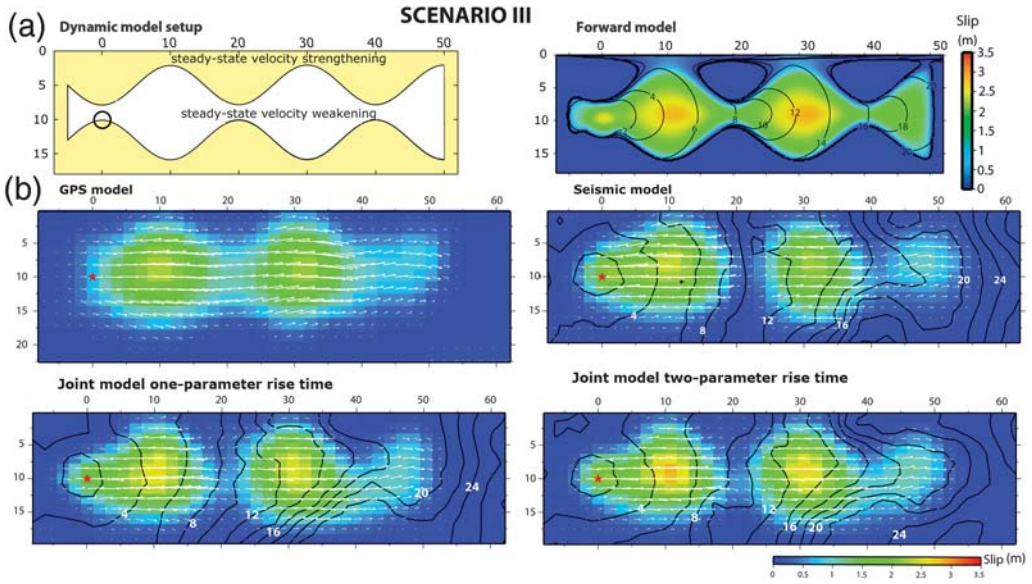

Figure 9. (a) The setup of scenario 3 for the dynamic rupture simulation (left) and resulting slip distribution with 2 s rupture time contours (right). (b) The slip distributions for the geodetic, seismic and two-joint inversions. Rupture time contours are shown for the kinematic inversions. Hypocenter is represented by a red star.

(Fig. 14a). The higher initial shear stress near the top and bottom boundaries of the velocity-weakening and velocity-strengthening zones is motivated by and qualitatively consistent with the prestress that naturally arises in models of earthquake sequences that incorporate interseismic stress build-up as well as co- and post-seismic stress changes (Kaneko and Lapusta, 2008; Lapusta and Liu, 2009). The result of this set up is a unilateral rupture toward east, with the rupture velocity transitioning from subshear to supershear due to the generalized Burridge–Andrews mechanism, the terminology used in Liu and Lapusta (2008). When the rupture reaches the bottom high-stress boundary between the rate-weakening and rate-strengthening zones it creates a supershear burst, followed by the original subshear rupture front. The magnitude of this event is M_w 7.37.

In our blind test, the kinematic modeling team started with the same assumptions as for the other scenarios and it could not produce a model that would fit the data well. Because of the greater complexity of this scenario, the number of stations was increased from 9 to 18 and stations closer to the fault plane were selected. When this station configuration was used, it became clear that the fits to the waveforms were progressively worse for the stations further away from the hypocenter. This gave the clue that the problem might be with the rupture velocity, which was 2–4 km/s to start with. When the range of rupture velocity was increased to 2–6 km/s (Table 1) and the number of stations was kept at 18, the earthquake was modeled successfully. The slip distribution is well determined in all inversions, although the abrupt tapering of slip at the bottom edge of the rupture is better retrieved with the waveform data than with the geodetic data (Fig. 14b). Figure 15 shows the L-curves used to determine the best-fit model. The choice of the model is again quite obvious.

Figure 16a shows the fits to the GPS data for the best-fitting joint model with two-parameter rise time, which shows that the fits are very good. Figure 16b shows the fits to the strong-motion data. It should be noted that both joint models fit the data from the stations close to the hypocenter near the western end of the fault. As the rupture propagates toward east, the quality of the fit deteriorates.

The rupture time contours of both seismic and joint inversions are also in broad agreement with the input model. In particular, the larger—supershear—rupture velocity of this scenario is captured by the inferred models. Figure 17 compares the slip-velocity snapshots of the input model and two joint models (saturated at 2 m/s). Because the parameterization of the kinematic modeling assumes a single rupture arrival time, the two rupture fronts, the one generated from the original subshear rupture and the other from the supershear daughter crack, cannot be resolved. This is likely the main reason for the fact that the quality of data fits get progressively worse for the stations that are closer to the end of the rupture (Fig. 16b). Still, as the snapshots reveal, the kinematic inversion attempts to mimic the two rupture fronts by significantly varying the rise time in such a fashion that the overall picture looks like a broad rupture front (Fig. 17). These rapid variations in rise time are the likely cause for the high frequency content in the kinematic model waveforms, which does not exist in the dynamic rupture simulation (Fig. 16b).

Scenario 5: Pulse-Like Rupture of Successive Asperities with a Random-Velocity Medium

In scenario 5, we further explore the influence of unmodeled heterogeneities of the velocity structure on inverted source parameters. We use the same source model as in

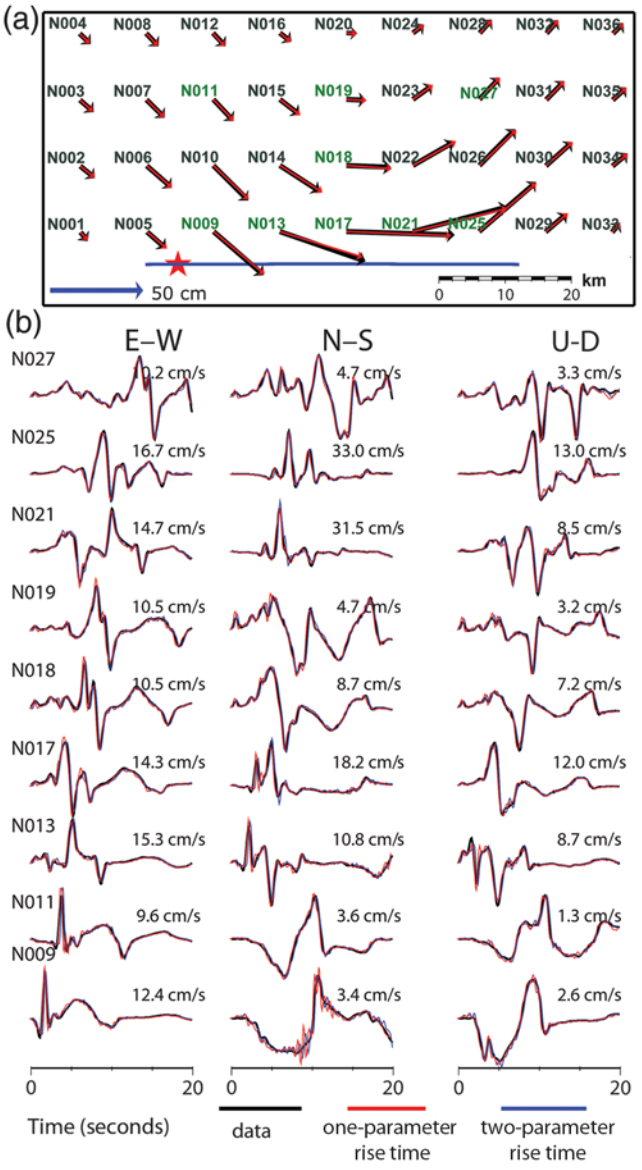

Figure 10. (a) The model roughness versus misfit curves (L-curves) for the geodetic and seismic data for scenario 3. The selected best-fit model is shown with a red circle. (b) The slip distributions for the two-parameter rise-time joint models with increasing model smoothness from top to bottom. The selected model is shown in a red rectangle.

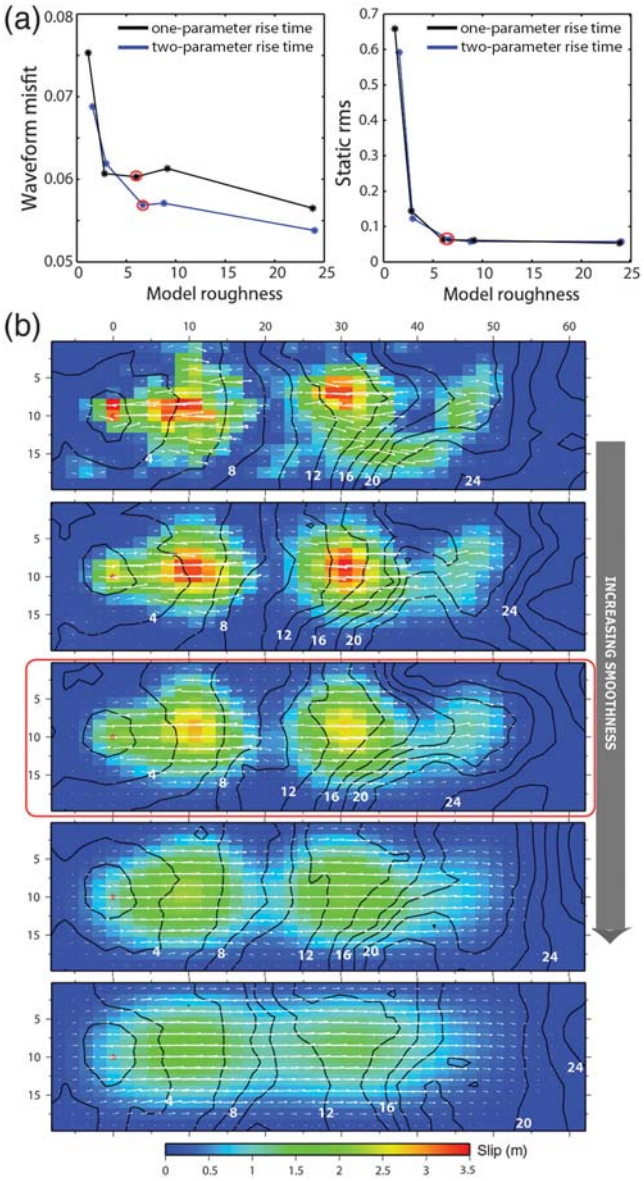

Figure 11. (a) Fits to the geodetic data for the best-fit joint model with two-parameter rise time for scenario 3. Data is in black and fits are in red. The station names are to the top left of the GPS data points. The name of the stations that are also used for seismic data are shown in green. The blue line shows the surface expression of the fault and red star represents the epicenter location. (b) Fits to the seismic data at nine stations for one-parameter (red) and two-parameter (blue) rise-time joint inversions.

scenario 3 except that a velocity structure in scenario 5 consists of a homogeneous half-space plus random fluctuations in seismic-wave speeds. We then invert for kinematic source parameters using Green's function computed from the homogeneous half-space. The random fluctuation is represented by a von Karman random function, which is defined as the Fourier transform of the correlation function given by (e.g., Hartzell *et al.*, 2010):

$$C_k \frac{1}{(1 + a_r^2 k_r^2)^{3/2+H}}, \tag{7}$$

in which C_k is a normalization constant, a_r is the correlation length, k_r is the radial wavenumber, and H is the Hurst exponent, which determines the spectral decay at high wavenumbers. Seismological studies show that observations of seismic-wave scattering and travel-time variations can be explained by a von Karman random medium with $H \approx 0$, the correlation length of the order of kilometers, and a standard deviation in velocity of about 5% (e.g., Frankel and Clayton, 1986). Hence, in our forward model, we set a Hurst exponent $H = 0$, the correlation length $a_r = 2$ km, and the standard deviation in velocity of 5% (Fig. 18a). We add these random

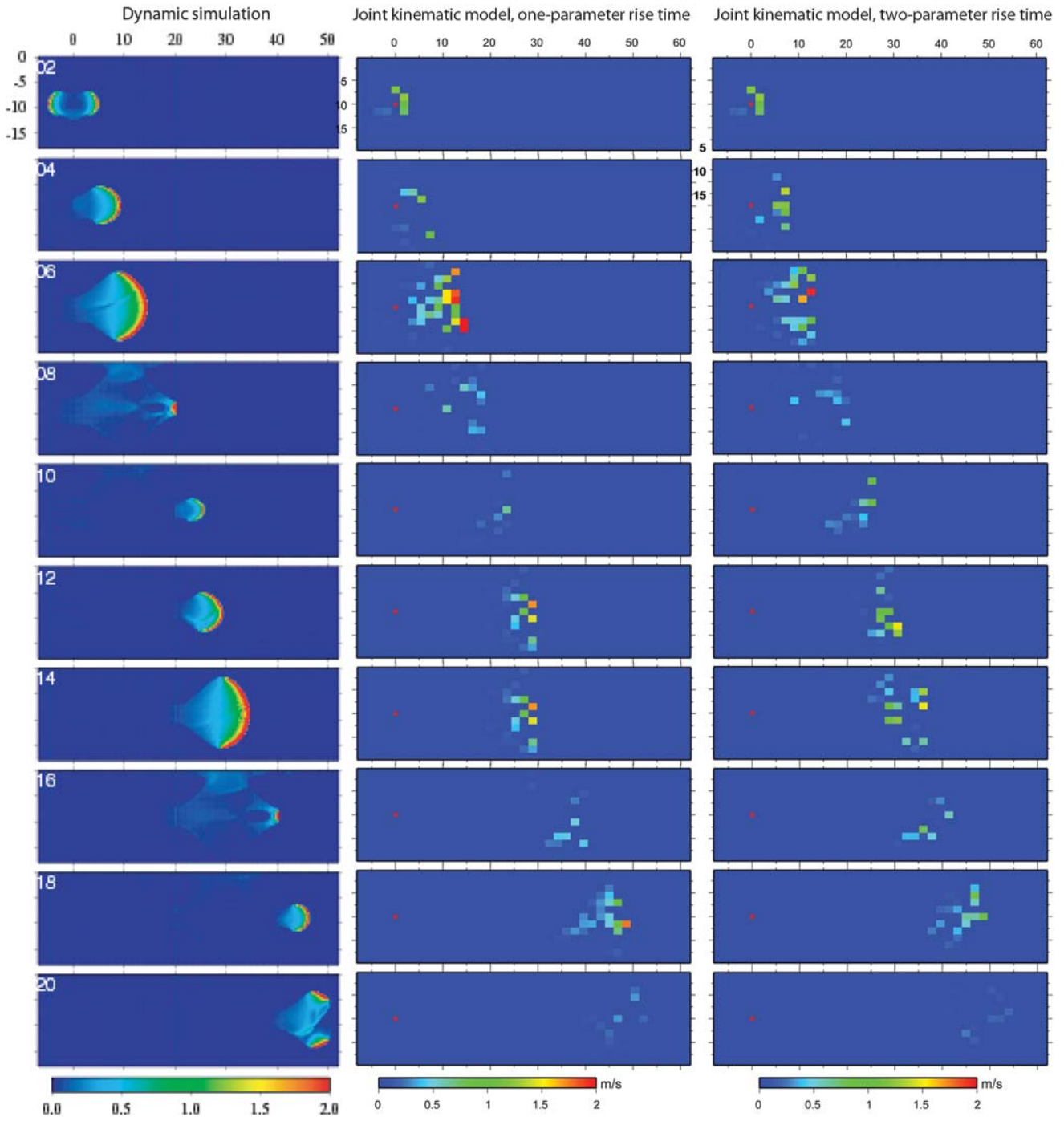

Figure 12. Snapshots of slip rate on the fault every 2 s for scenario 3 for the input model (left), joint model with one-parameter rise time (center) and joint model with two-parameter rise time (right). The velocities are saturated at 2 m/s.

perturbations to the *P*- and *S*-wave velocities while the density is unperturbed.

With the heterogeneity in the velocity structure, 1% larger prestress is needed for the dynamic rupture to propagate over the velocity-weakening region as in scenario 3. The resulting slip distribution in scenario 5 is slightly different from that of scenario 3, but the essential features of the source model remain unchanged (Fig. 18a and Table 2).

The inversion results show that, despite the inaccurate 1D Green's functions used for the modeling, the slip distribution and rupture velocity is well modeled using seismic and joint inversions (Fig. 18). The estimates of average and peak slip, and stress drop are also in the similar range of accuracy with respect to the other four scenarios and especially to scenario 3, which has similar slip distribution and rupture history (Table 2). The process of selecting the preferred

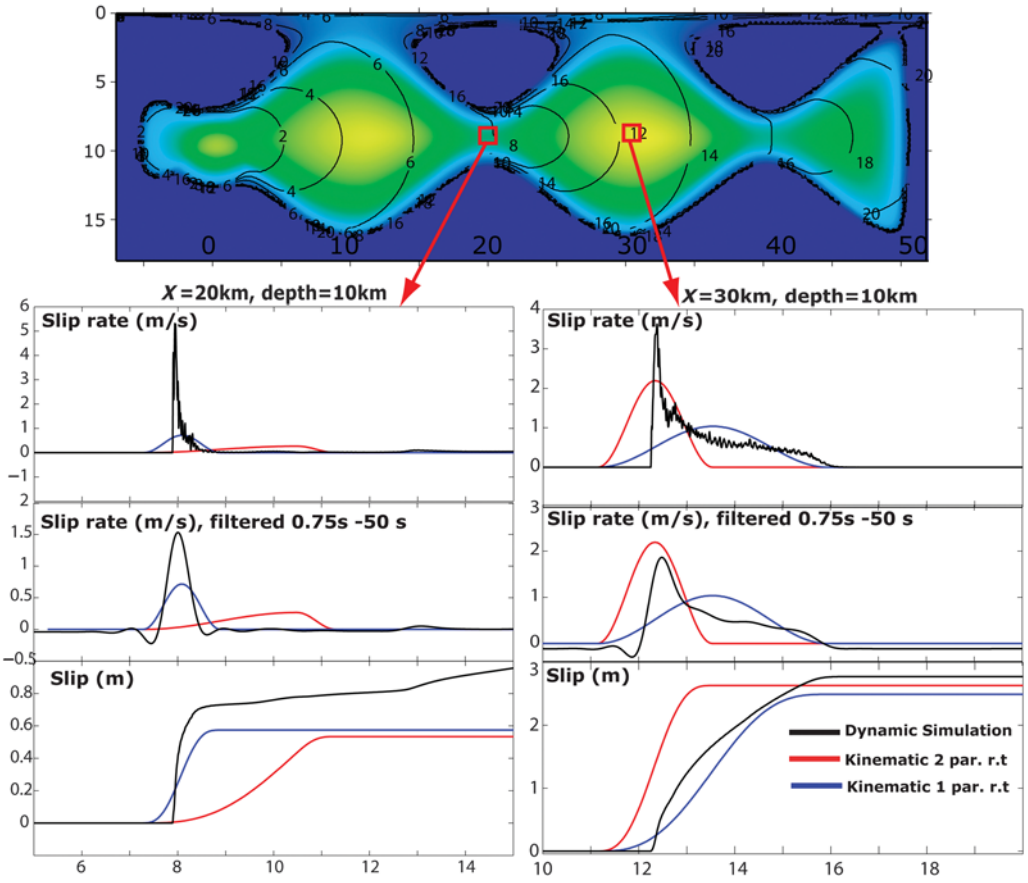

Figure 13. The slip history of two points on the fault plane ($X = 20$ km, $Z = 10$ km and $X = 30$ km, $Z = 10$ km) for scenario 3. The top plot shows the unfiltered slip rate of the input model (black) and the one-parameter (blue) and two-parameter (red) rise-time joint models. The middle plots show the slip rate filtered in the bandwidth of the inversion (0.75–50 s). The bottom plots show the evolution of slip.

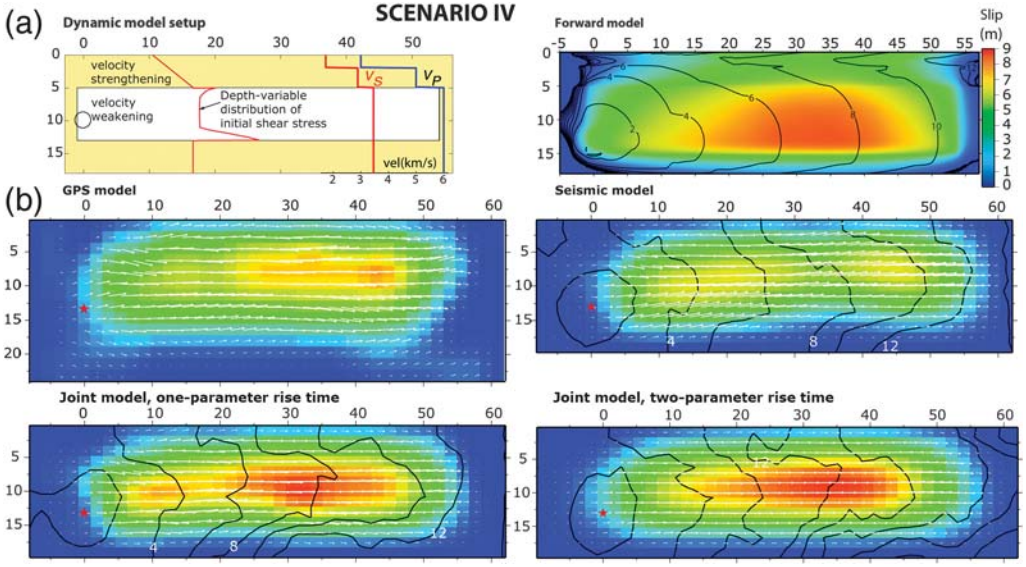

Figure 14. (a) The setup of scenario 4 for the dynamic rupture simulation (left) and resulting slip distribution with 2 s rupture time contours (right). The velocity model (V_P and V_S) and the initial shear stress distribution is also shown (left). (b) The slip distributions for the geodetic, seismic, and two-joint inversions. Rupture time contours are shown for the kinematic inversions. Hypocenter is represented by a red star.

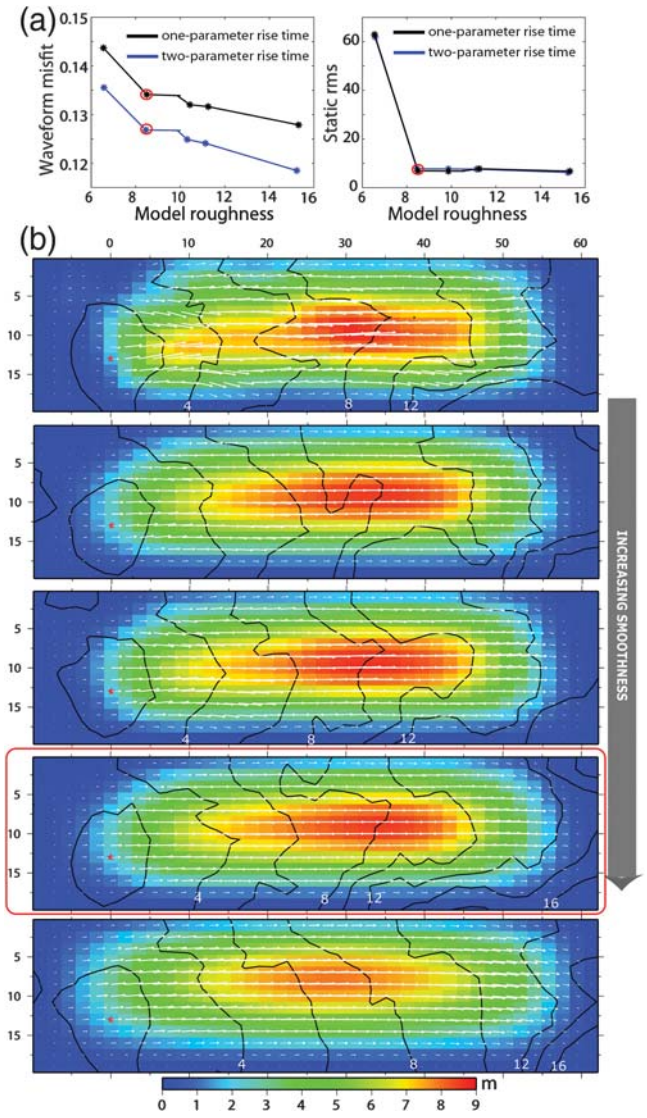

Figure 15. (a) The model roughness versus misfit curves (L-curves) for the geodetic and seismic data for scenario 4. The selected best-fit model is shown with a red circle. (b) The slip distributions for the two-parameter rise-time joint models with increasing model smoothness from top to bottom. The selected model is shown in a red rectangle.

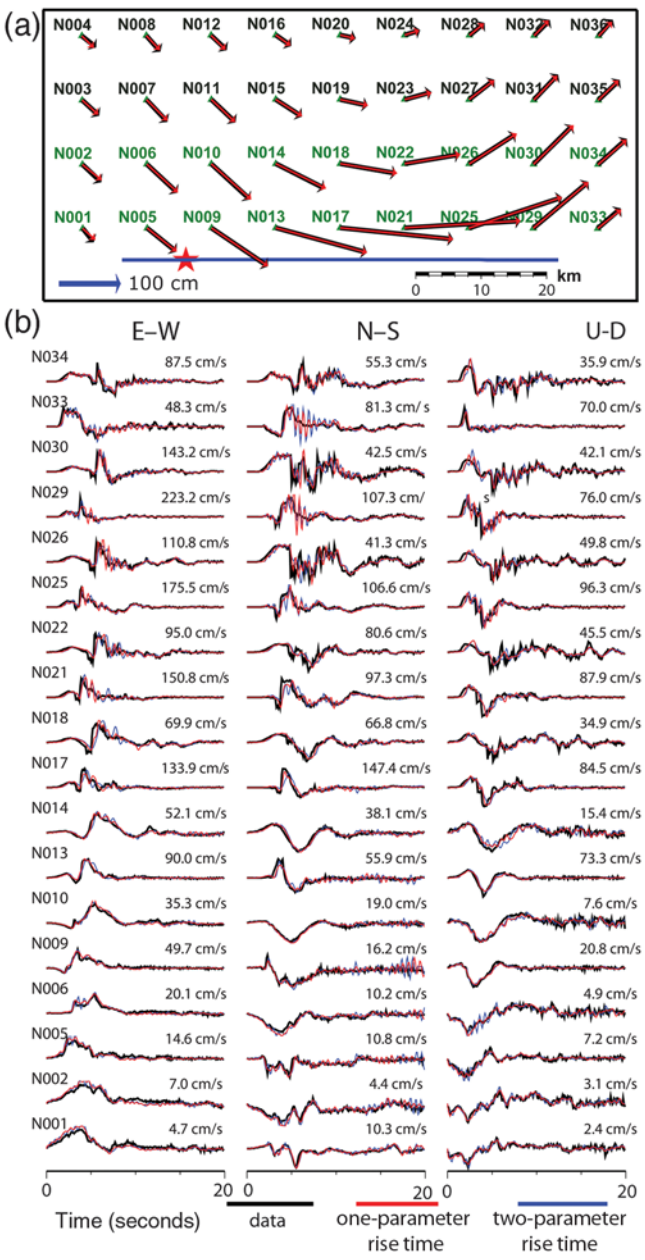

Figure 16. (a) Fits to the geodetic data for the best-fit joint model with two-parameter rise time for scenario 4. Data is in black and fits are in red. The station names are to the top left of the GPS data points. The name of the stations that are also used for seismic data are shown in green. The blue line shows the surface expression of the fault and the red star represents epicenter location. (b) Fits to the seismic data at 18 stations for one-parameter (red) and two-parameter (blue) rise-time joint inversions.

model from the L-curves is also quite similar to the one in scenario 3 (Ⓔ Fig. S2 available in the electronic supplement to this article). The major difference is the quality of fits to the seismic data as shown by the lower variance reduction (Table 2) and fits to the seismic data (Ⓔ Fig. S3 available in the electronic supplement to this article). The arrival times of the *S*-wave phases are incorrectly reproduced at some stations further away from the fault. The geodetic fits are not affected as much by the inaccuracy of the Green's functions (Table 2, Ⓔ Fig. S2 available in the electronic supplement to this article) due to relative insensitivity of geodetic data to the 3D structure (Wald and Graves, 2001). The snapshots show that the overall rupture history can be obtained with a similar level of accuracy (Ⓔ Fig. S4 available in the electronic supplement to this article) compared to scenario 3 (Fig. 12).

Discussion

Resolution of Slip Distribution

The slip distribution is well determined in all five rupture scenarios. The maximum and average slip values

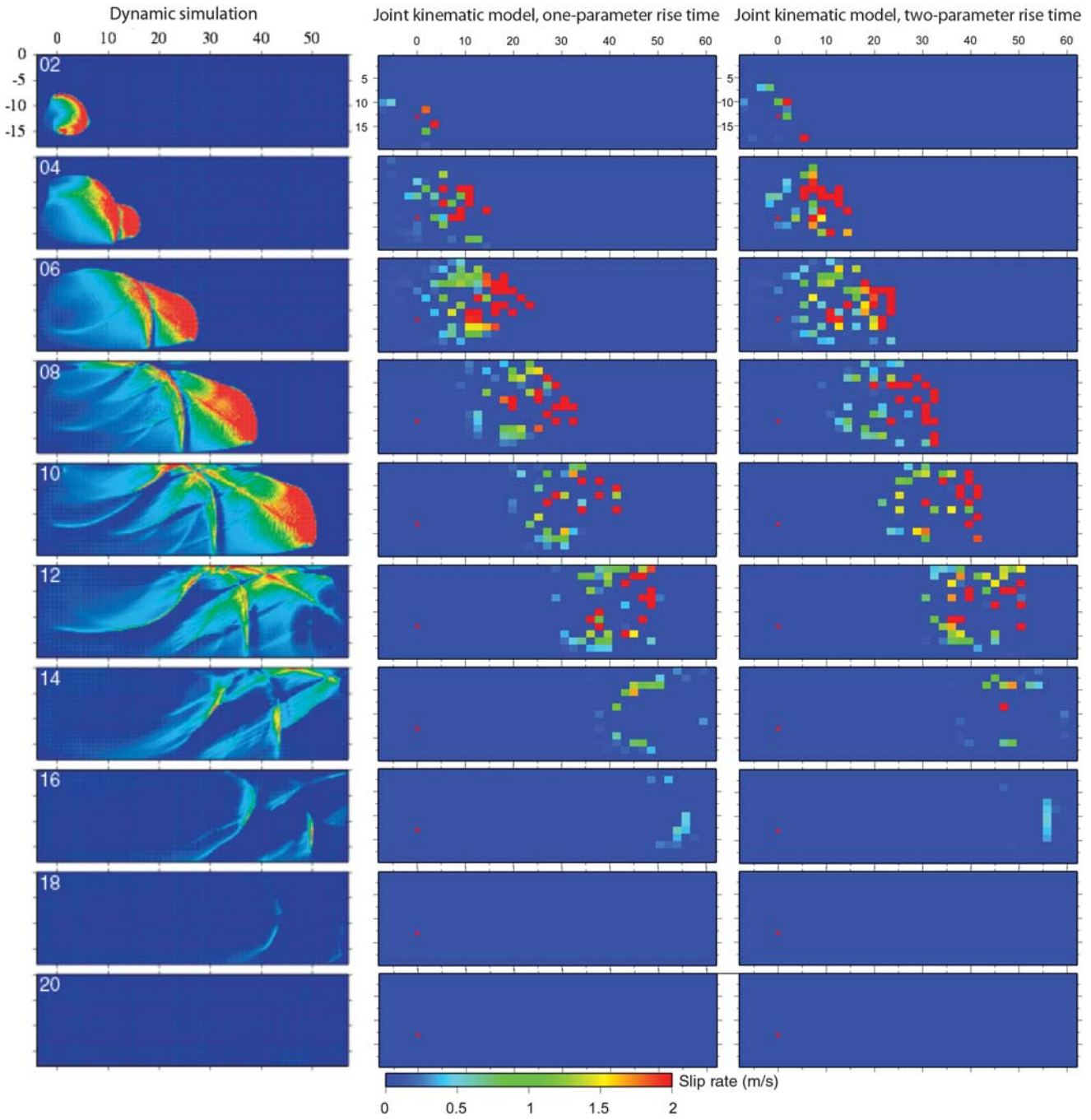

Figure 17. Snapshots of slip rate on the fault every 2 s for scenario 4 for the input model (left), joint model with one-parameter slip function (center) and joint model with two-parameter slip function (right). The velocities are saturated at 2 m/s.

determined from the inversions differ from the input values by at most 30%, and by less than 5% in some cases (Table 2). The well-known lack of depth resolution of geodetic data (e.g., Bos and Spakman, 2003; Page *et al.*, 2009) is observed in these examples. We also see that the inversion of the waveforms does alleviate this limitation to some degree, with generally a better rendering of the longer wavelengths of the slip distribution. The static displacements are beneficial for constraining the along-strike variations of slip, because the resolution of strong-motion data decreases as the rupture propagates away from the hypocenter (Custodio *et al.*, 2009).

Resolution of Rupture Velocity

We compute depth-averaged 1D rupture arrival times for both the input and inverted models in each scenario based on the arrival of rupture front (Fig. 19). The rupture velocity is reasonably well resolved for three of the four scenarios. In

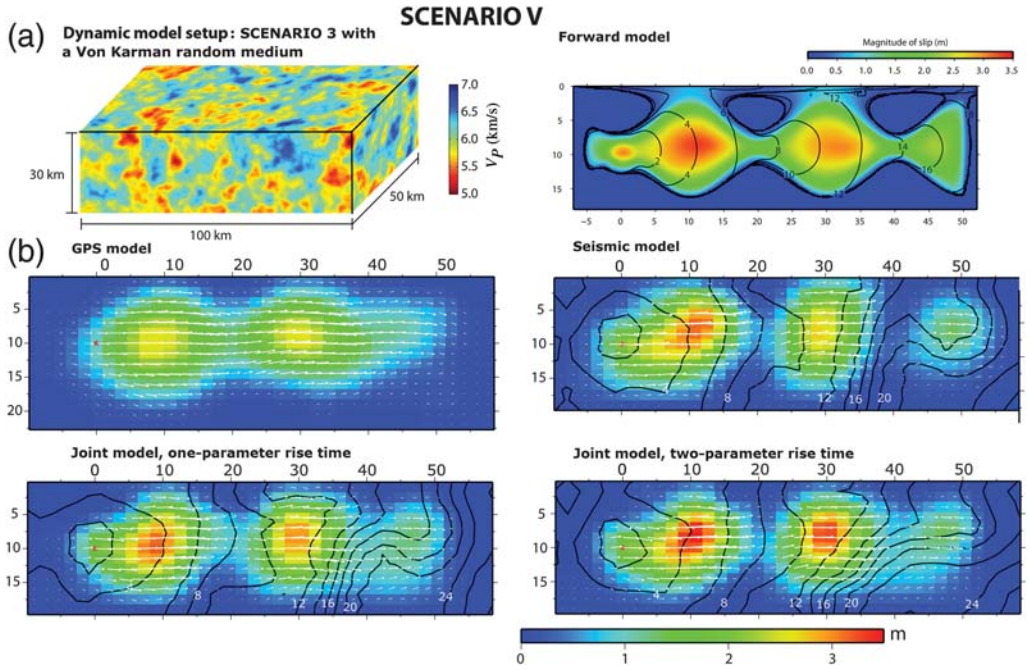

Figure 18. (a) The setup of scenario 5 for a 3D random bulk velocity variation and resulting slip distribution with 2 s rupture time contours (right). We use a von Karman random medium with a Hurst exponent $H = 0$, the correlation length $a_r = 2$ km, and the standard deviation in V_P of 5%. We assume that $V_S = V_P/3$. (b) The slip distributions for the geodetic, seismic, and two-joint inversions. Rupture time contours are shown for the kinematic inversions. Hypocenter is represented by a red star.

particular, the inversion procedure is capable of distinguishing between the subshear propagation in scenarios 1–3 and supershear propagation in scenario 4, as highlighted in Figure 19 in which scenarios 3 and 4 are plotted together. We conclude that significant changes of rupture velocity, including the supershear and subshear segments, can be resolved given sufficient data to limit the trade-off between the model parameters. The rupture arrival times show that, as the rupture propagates away from the hypocenter, the estimates of rupture velocity deteriorates. The inversion results seem to be delayed. This deterioration is the worst in scenario 2 as also seen from the rupture contours (Fig. 5). This is possibly due to interfering phases coming from the other rupturing points, which decrease resolution of the seismic data as rupture moves away from the hypocenter. We hypothesize that this problem can be resolved by increasing the weight on the time smoothness in the objective function (equation 6) such that the rupture velocity is controlled by the initial parts of the seismograms and then kept almost constant unless data necessitates a significant shift.

The isochrones of the rupture front are unstable because the rupture velocity is not resolved for the sections that do not slip significantly. The evolution of the rupture front is clearer from the snapshots of slip velocity on the fault. It should be noted that, following the common practice in earthquake source studies, the absolute timing of the seismograms are not utilized due to limitations of the inversion code. If absolute timing were used in conjunction with accurate seismic-velocity models, it would help constrain the rupture velocity better. However, this requires a detailed knowledge of the velocity structure around the source which generally is not available with sufficient accuracy. Therefore, it is customary to align the waveforms on their first arrival times, as done in this study.

Resolution of Average Stress Drop

The values of stress drop inferred from the kinematic models are similar to those of the input dynamic models (Table 2), though slightly smaller (by typically 10%–30%) in most cases considered. To compare the same stress-drop measure in both the input and inverted models, we compute the average stress drop using an analytical solution for a rectangular fault of length l and width w in the case in which $l \gg w$ (Knopoff, 1958; Madariaga, 1977), using

$$\Delta\sigma = \frac{2}{\pi}\frac{M_0}{Aw}, \tag{8}$$

in which M_0 is the moment, A is the effective area, and w is the fault width. Different ways of computing the average stress drop are discussed in Noda *et al.* (2013). The difference between stress drops computed from the input and inverted models can partly be explained by the smoothing of the slip distribution during an inversion process, resulting in a larger rupture area and hence lower stress drop.

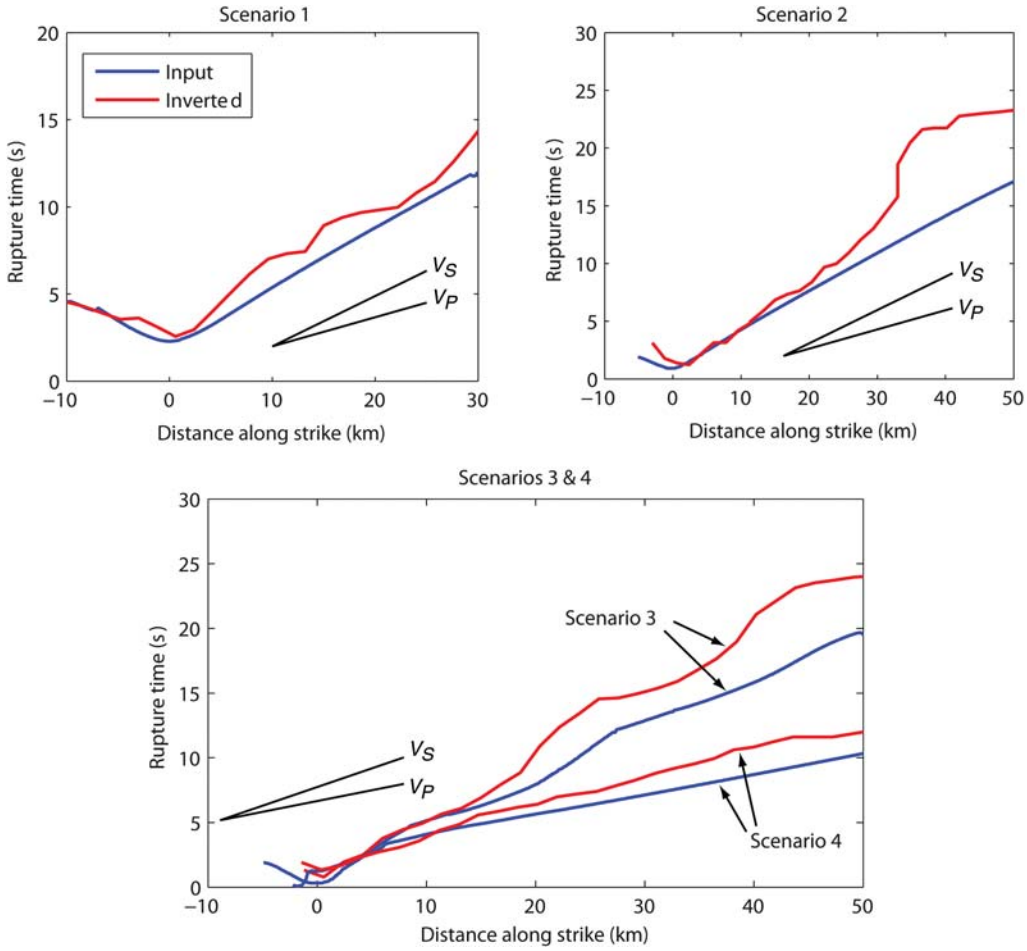

Figure 19. Comparison of rupture front propagation between the input (blue) and inverted models (red) for scenarios 1–4. Depth-averaged 1D rupture arrival times as a function of distance along strike are plotted. The rupture time is defined as the time when slip rate first exceeds 1 mm/s for the input dynamic model and the time when slip rate first becomes nonzero for the inverted model, respectively. We compute depth-averaged rupture times using subfaults that slip more than 30% of the average slip.

Resolution of Rise-Time Function

The shape and width of the slip function at each point on the fault is the most difficult to resolve amongst the source parameters (Guatteri and Spudich, 2000). Cohee and Beroza (1994) showed that for the 1992 Landers earthquake, one can model the data well using either short or long rise times, and hence the details of the rise time are hard to resolve. It is also part of the critical information that should be retrieved in order to investigate fault friction laws. The slip rates resulting from dynamic modeling usually have a Kostrov-type shape with fast acceleration and slower deceleration (Tinti *et al.*, 2005), and this has motivated the use of the two-parameter rise-time function described in equation (3). For kinematic inversions some choose to define rise-time functions with a few parameters such as a single-parameter smoothed ramp (Cotton and Campillo, 1995), one-parameter cosine function (Ji *et al.*, 2002), two-parameter cosine function (Liu *et al.*, 2006), and truncated square root singularity (Beroza and Spudich, 1988), while others use rise-time functions with more parameters such as multiple time window triangles (Hartzell

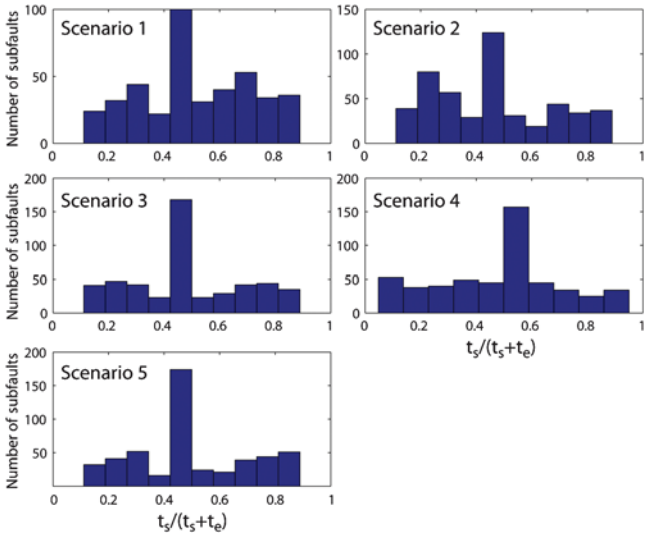

Figure 20. Histogram of ratio of the duration of acceleration phase (t_s) of the rise time to total rise time ($t_s + t_e$) at each subfault for the best-fit kinematic models that use the two-parameter rise-time function for the scenarios 1–5.

and Heaton, 1983; Wald and Heaton, 1994) and multiple time window triangles with smoothing (Sekiguchi *et al.*, 2000).

We use the example of scenario 3 to comment in more detail on the ability of our inversion procedure to retrieve the history of slip at the rupture front. To do so, we compare the input and inverted slip history at one point on the fault at the center of the second large asperity (Fig. 13). The simplified shape of the rise-time function approximates only crudely the asymmetric slip history of the dynamic model (Fig. 13). In addition, the filtering of the waveforms precludes retrieving the abrupt increase of slip velocity at the rupture front. To assess the information lost due to the filtering, we also compare the inverted slip history at this point with the filtered slip history of the dynamic model (0.75–50 s). This comparison is more relevant to assess the effect of the inversion procedure as it takes into account the limitation introduced by the limited bandwidth of the synthetic data used in the inversion. In this case, we see that the amplitudes of slip velocities in the input and inverted models are of the same order of magnitude. However, it clearly demonstrates that the smooth rendering of the slip-history is not only due to the filtering of the waveforms but also due to the assumed shape of the rise-time function. We observe that the two-parameter rise-time function does not yield much improvement over the simpler one-parameter rise-time function. In fact, we generally find that the asymmetry between the slip velocity increase and decrease, observed in dynamic rupture models, could not be retrieved well even with this two-parameter rise-time function. Figure 20 shows the histogram of the inverted best-fit distribution of the ratio of the velocity increase portion (t_s in equation 3) rise time ratio to the total duration of the rise time for the five scenarios ($t_s + t_e$ in equation 3) of this study. If, on average, the inverted rise times contained the asymmetry observed in the dynamic rupture simulations, the significant portion of the ratios would be below 0.5. However, most of the ratios are around 0.5 and values lower and higher than 0.5 are about equally likely (Fig. 20), showing that the two-parameter rise-time function does not lead to models with a sharper acceleration and slower deceleration of the rise time.

Ⓔ Figure S5 (available in the electronic supplement to this article) shows the high frequency (0.5–4 Hz) content of seismograms of the dynamic simulation and kinematic inversion with two-parameter rise time for the scenario 1. This comparison further illustrates the difficulty of modeling the high-frequency content. The sharpest phases that appear at the stations very close to the fault rupture (e.g., N013 and N017) are not explained by our kinematic models. This sharp high-frequency phase is due to the rapid acceleration at the onset of sliding in the dynamic rupture simulation. These sharp phases are not reproduced well because their frequency content is mostly outside the range of the frequency band of the kinematic inversions. In addition, they account for only a small fraction of the signal in the seismogram. So, unless special weight is given to these phases, they cannot be retrieved from our inversion procedure.

An implication of the fact that kinematic source models do not resolve well the slip variations at high frequency is that the rupture velocity defined in kinematic source models does not necessarily represent the rupture velocity of dynamic source models as the rupture times are actually defined differently. In dynamic simulations the rupture time is naturally defined as the time of first-break of the Kostrov-like slip function, while in kinematic source model it is the onset of the low-frequency wavelet tracked in the inversion procedure as evident in Figure 13 (see Oglesby and Mai [2012] for a detailed discussion of this issue).

It must be noted that, because there is no smoothing of rise time, the values of rise time can vary significantly along the fault in the kinematic inversions, even in the neighboring subfaults with similar slip amplitudes. Such a feature is not seen in the dynamic rupture simulations considered in this study. Although the substantial variations in the rise time may be produced in a dynamic rupture model in which points next to each other have very different frictional properties or prestress, such models are also likely to result in heterogeneous slip; smooth slip along with rapidly varying rise-time functions may not be physically plausible. Our results suggest that it would be better or at least more consistent, to impose smoothing on the rise-time distribution in kinematic inversions while still keeping one- or two-parameter descriptions for rise-time function, unless data is sufficient and involves complexities that require multiple time windows.

In the cases of multiple rupture fronts, as in scenario 4, inversions with single-time-window approaches would be inadequate. However, if there is sufficient data coverage, the progressive deterioration of the fit between the data and the synthetic waveforms away from the hypocenter is an indication that the rupture history is more complicated than the single rupture pulse allowed by the formalism used in the inversion. In other words, the quality of fits to the data could be used as a factor determining whether or not the rupture history has unforeseen complications.

Resolution of Rise Time and Crack- Versus Pulse-Like Ruptures

Rise time is an important parameter. Earlier teleseismic studies suggested that the rise-time scales with the size of the fault (Geller, 1976). However, as Heaton (1990) pointed out, near-field strong-motion records suggest that rise times are an order of magnitude smaller than the overall duration of large earthquakes. Whether we can resolve the slip zone width, and hence whether we can tell the difference between a crack and a pulse, is a question of critical importance for earthquake source physics.

The first two inversion tests of this study have been designed to investigate whether the kinematic inversion models can resolve pulse-like versus crack-like ruptures or, more generally, scenarios with different rise times. In scenario 1, the broad seismogenic zone leads to a long rise-time characteristic of a crack-like rupture. In scenario 2, because the

seismogenic zone is much narrower, the stopping phases from the boundaries of this narrow zone lead to much shorter rise times. In most kinematic inversion codes, including the one used in this study, a certain range of possible rise times is prescribed to start with, making the code invert for a pulse. With such assumptions, it would not be possible to invert for a crack-like rupture. However, the comparison of strong-motion data of the two scenarios does show that the crack-like rupture creates distinctively broader waveforms than the pulse-like rupture (Figs. 3b; 7b). Despite the formalism being biased toward pulse-like ruptures, our inversions succeed in reproducing this difference. As a result, the inverted widths of the slipping zone in scenario 1 are significantly broader than in scenario 2.

The Effect of Imprecisely Known Green's Functions

Our results from scenario 5 show that relatively small inaccuracies in the Green's functions do not substantially affect the inversion results, at least for the relatively smooth scenario considered here. Although the scenario earthquake and data are created in a half-space model with seismic velocity perturbation of 5% standard deviation, the inversion with Green's functions for a uniform half-space determines the earthquake kinematics to a similar level of accuracy as in scenario 3, in which the exact same Green's functions are used both for computing the synthetics and in the inversion procedure. However, the inaccuracies of Green's functions in scenario 5 are evident from the mistiming of seismic phases and the lower variance reduction of seismic data (Ⓔ Fig. S3 available in the electronic supplement to this article; Table 2).

The addition of geodetic data improves the slip model quite efficiently (Fig. 18). Although the inaccuracy of the Green's functions leads to significantly lower variance reduction to seismic data, the fit to the geodetic data does not change much (Table 2). This is due to the well-known relative insensitivity of geodetic data to 3D elastic heterogeneities (Wald and Graves, 2001). The static displacement measured at a geodetic station is indeed sensitive to the elastic properties averaged between the measurement point and the slip zone at depth. In the absence of large-scale 3D heterogeneities, an average 1D model is generally sufficient to fit geodetic data.

This test shows that, if there is a good coverage of seismic and geodetic stations close to the fault and the average 1D Green's functions are correctly determined, 3D heterogeneities of the elastic properties of up to 5% would not deteriorate the slip model significantly. This conclusion would likely not hold for higher amplitude perturbations, or an inadequate 1D average model, or large-scale heterogeneities that would not be averaged out by the large number of near-field data considered in this analysis (Graves and Wald, 2001; Wald and Graves, 2001; Liu and Archuleta, 2004).

Insights on Improving Kinematic Inversions of Earthquakes

In this study, the ill-posed problem of the inversion of a finite-fault earthquake source model is regularized by the choice of a particular formalism which assumes a single rupture front determined by a rupture velocity and a rise-time function with a fixed simple functional shape and constrained duration. These critical assumptions significantly constrain the space of possible solutions, but our study shows that this approach still allows a reasonably well recovery of some of the key features relevant to the physics at play in seismic ruptures propagation, at least for the relatively simple ruptures considered in this study.

One approach to limit the possible solutions is the smoothing of source parameters. Smoothing of slip of neighboring subfaults is almost ubiquitous among kinematic modeling approaches. However, smoothness of slip only, is not the only criterion for the smoothness of a spatiotemporal model; one can smooth the slip, yet have roughness of slip functions or rapid changes in rupture velocity. The inversion approach used in this study does include a time smoothness term which penalizes deviation from a constant rupture velocity (Shao *et al.*, 2011). However, following Ji *et al.* (2002), our inversion approach keeps the shape of the rise-time function the same, but lets the duration vary in a range without any correlation between neighboring subfaults. While this is clearly a more general, and hence more preferable, assumption than assuming a single rise time with just a single unique duration for the entire fault (e.g., Bouchon *et al.*, 2002). It is also clear that there is not enough resolution for the rise-time function to be determined separately for each subfault. If the rise time is allowed to rapidly vary, and given the smoothing imposed on slip and rupture velocity, the high-frequency content of the data are mapped into rapid variations of rise time. By smoothening the rise time as well, one could suppress the possibility of generating the high-frequency content of the waveforms with spurious variations of rise time. Hence we propose to add another factor to the cost function that involves the smoothing of amplitude of slip divided by rise time for neighboring subfaults similar to the slip and rupture velocity smoothing. This may lead the inversion code to sharpen the pulse shape instead, in order to match those high frequencies.

Another lesson concerns the single-window restriction on the slipping zone: if the data implies a more complex evolution of rupture, in the sense that a single-window inversion produces a systematic mismatch to the data, then one should use a multiple-window inversion (e.g., Sekiguchi and Iwata, 2002; Dunham and Archuleta, 2004). Multiple-window inversions impose causality and smoothness, solve for the evolution of rupture, allow the slip at each point to be determined by multiple time window functions with no predetermined shape, calculate the rupture velocity, and observe the slip functions *a posteriori*. Moreover, in some cases, the multiple time window approach is used with linearized

inversion (e.g., Hartzell and Heaton, 1983; Sekiguchi *et al.*, 2000), which requires a constant rupture velocity and attributes all of the seismogram complexities to complexities of source time functions and slip. Hartzell *et al.*, (2007) studied the 2004 Parkfield earthquake using both nonlinear two-parameter rise time and a linear multiwindow approach. In the case of the Parkfield earthquake, in which rupture velocity is almost constant and there is a dense coverage of stations, both methods yielded similar slip models. However, unless there is high density of stations, this leads to problems with estimating rupture velocity, slip distribution, and moment of the earthquake (Cohee and Beroza, 1994; Cotton and Campillo, 1995). In that light, assuming a simple rise-time function defined by only one or two parameters in an inversion procedure that allows us to capture rupture-speed variations may be desired. Overall, the best approach may be to conduct inversions with different sets of clearly understood assumptions (single versus multiple windows, variable versus constant rupture speed) and then have several potential versions of what may have occurred in a given event. The plausibility of those versions can then be studied using physics-based earthquake models.

Another possibility is to invert for dynamic parameters directly. Such inversions based on dynamic-rupture models have been attempted for several large earthquakes (Olsen *et al.*, 1997; Carli *et al.*, 2010). Inverted slip models are dynamically consistent with and may be more realistic than those obtained by kinematic models. However, such inversions generally pose a major computational challenge even with a reduced set of model parameters. The number of model parameters typically scales with the number of available strong-motion records. Hence with abundant data, for example, as in the case considered in this study, the number of model parameters sufficient to resolve the details of the input source models may become intractable. In addition, dynamic inversions also suffer from some fundamental trade-offs between strength excess and slip-weakening distance, and from similar problems with estimating slip histories for points on the fault (Guatteri and Spudich, 2000; Goto and Sawada, 2010).

Conclusion

We have produced various rupture scenarios using dynamic rupture simulations, and inverted the resulting waveforms and static data using a kinematic inversion code. Our study shows that, for these idealized cases with no noise, known fault geometry, known or nearly known bulk properties, and sufficient data coverage, current kinematic inversion schemes are performing well at estimating the slip distribution, average stress drop, and rupture velocity. The geodetic models capture the overall features of the slip distribution well (moment in particular) but short wavelengths are always smoothed out due to the regularization procedure. Including the seismic waveforms in the inversion helps resolve better the short wavelengths and provides relatively reliable estimates of the propagation of the rupture front. The heuristic way of choosing the best-fit model using L-curves seems to work in the cases of relatively smooth slip variations presented here.

However, even for the idealized cases discussed here, the slip function and rise time are harder to resolve, and much caution must be taken in interpreting slip-history retrieved form kinematic inversion in terms of fault friction. Because of the parameterization used in our inversion procedure, the inverted sources are biased to be pulse-like ruptures, although often they are not as short in duration as the input source. The regularization introduces some smoothing leading to more symmetrical rupture front and lower-slip velocity than in the input model. An implication is that the slip distances over which friction evolves on the fault would be likely overestimated, as pointed out in previous studies (Guatteri and Spudich, 2000).

Simply increasing the number of parameters used to describe the slip function does not yield any significant improvement. To add constraints on the shape of the slip functions, inversions may benefit from spatial smoothing of inferred slip function parameters such as rise time and from optimizing the misfit function so as to be more sensitive to beginnings of seismograms.

Data and Resources

No data were used in this paper. Some plots were made using the Generic Mapping Tools version 4.2.1 (www.soest.hawaii.edu/gmt; Wessel and Smith, 1998) and MATLAB (version 7).

Acknowledgments

This study was supported by the National Science Foundation (NSF) (Grant EAR 0548277 to NL), and partially funded by the Gordon and Betty Moore Foundation through Grant GBMF Number 423.01 to the Caltech Tectonics Observatory, and the Southern California Earthquake Center (SCEC). This is Caltech Tectonics Observatory Contribution Number 228. SCEC is funded by NSF Cooperative Agreement EAR-0106924 and U.S. Geological Survey Cooperative Agreement 02HQAG0008. Numerical simulations for this study were performed on the CITerra Dell cluster at the Division of Geological and Planetary Sciences of the California Institute of Technology. This manuscript has benefited from thoughtful suggestions and detailed comments by our reviewers, P. Martin Mai, and one anonymous reviewer.

References

Ampuero, J. P. (2002). Etude physique et numérique de la nucléation des séismes, *Ph.D. Thesis*, Univ. Paris 7, Denis Diderot, Paris (in French).

Andrews, D. J. (1976). Rupture propagation with finite stress in antiplane strain, *J. Geophys. Res.* **81,** no. 20, 3575–3582.

Archuleta, R. (1984). A faulting model for the 1979 Imperial Valley earthquake, *J. Geophys. Res.* **89,** 4559–4585.

Beresnev, I. (2003). Uncertainties in finite-fault slip inversions: To what extent to believe? (a critical review), *Bull. Seismol. Soc. Am.* **93,** no. 6, 2445–2458.

Beroza, G., and T. Mikumo (1996). Short slip duration in dynamic rupture in the presence of heterogenous slip properties, *Bull. Seismol. Soc. Am.* **101,** no. B10, 22,449–22,460.

Beroza, G., and P. Spudich (1988). Linearized inversion for fault rupture behavior: Application to the 1984 Morgan Hill, California earthquake, *J. Geophys. Res.* **93,** no. B6, 6275–6296.

Bos, A. G., and W. Spakman (2003). The resolving power of coseismic surface displacement data for fault slip distribution at depth, *Geophys. Res. Lett.* **30,** no. 21, doi: 10.1029/2003GL017946.

Bouchon, M., M. P. Bouin, H. Karabulut, M. N. Toksoz, M. Dietrich, and A. J. Rosakis (2001). How fast is rupture during an earthquake? New insights from the 1999 Turkey earthquakes, *Geoph. Res. Lett.* **28,** no. 14, 2723–2726.

Bouchon, M., M. N. Toksoz, H. Karabulut, M. P. Bouin, M. Dietrich, M. Aktar, and M. Edie (2002). Space and time evolution of rupture and faulting during the 1999 Izmit (Turkey) earthquake, *Bull. Seismol. Soc. Am.* **92,** no. 1, 256–266.

Carli, S. D., C. Francois-Holden, S. Peyrat, and R. Madariaga (2010). Dynamic inversion of the 2000 Tottori earthquake based on elliptical subfault approximation, *J. Geoph. Res.* **115,** no. B12328, doi: 10.1029/2009JB006358.

Cocco, M., and A. Bizzarri (2002). On the slip-weakening behavior of rate- and state dependent constitutive laws, *Geophys. Res. Lett.* **29,** no. 11.

Cohee, B., and G. Beroza (1994). Slip distribution of the 1992 Landers earthquake and its implications for earthquake source mechanics, in *Special Issue on 1992 Landers Earthquake Sequence*, special issue, *Bull. Seismol. Soc. Am.* **84,** 692–712.

Cotton, F., and M. Campillo (1995). Frequency-domain inversion of strong motions–Application to the 1992 Landers earthquake, *J. Geophys. Res.* **100,** no. B3, 3961–3975.

Custodio, S., M. T. Page, and R. J. Archuleta (2009). Constraining earthquake source inversions with GPS data 2: A two-step approach to combine seismic and geodetic datasets, *J. Geophys. Res.* **114,** no. B01315, doi: 10.1029/2008JB005746.

Day, S. M., L. A. Dalguer, N. Lapusta, and Y. Liu (2005). Comparison of finite difference and boundary integral solutions to three-dimensional spontaneous rupture, *J. Geophys. Res.* **110,** no. B12307, doi: 10.1029/2005JB003813.

Delouis, B., D. Giardini, P. Lundgren, and J. Salichon (2002). Joint inversion of InSAR, GPS, teleseismic, and strong-motion data for the spatial and temporal distribution of earthquake slip: Application to the 1999 Izmit mainshock, *Bull. Seismol. Soc. Am.* **92,** no. 1, 278–299.

Dieterich, J. (1978). Time-dependent friction and the mechanics of stick-slip, *Pure Appl. Geophys.* **116,** no. 4–5, 790–806.

Dieterich, J. H. (1979). Modeling of rock friction, 1, experimental results and constitutive equations, *J. Geophys. Res.* **84,** 2161–2168.

Dunham, E., and R. Archuleta (2004). Evidence for a supershear transient during the 2002 Denali fault earthquake, *Bull. Seismol. Soc. Am.* **94,** no. 6B, S256–S268.

Frankel, A., and R. Clayton (1986). Finite difference simulations of seismic scattering: Implications for the propagation of short-period seismic waves in the crust and models of crustal heterogeneity, *J. Geophys. Res.* **91,** no. B6, 6465–6489.

Geller, R. (1976). Scaling relations for earthquake source parameters and magnitudes, *Bull Seismol. Soc. Am.* **66**.

Goto, H., and S. Sawada (2010). Trade-offs among dynamic parameters inferred from results of dynamic source inversion, *Bull. Seismol. Soc. Am.* **100,** no. 3, 910–922.

Graves, R. W., and D. J. Wald (2001). Resolution analysis of finite fault source inversion using one- and three-dimensional Green's functions 1. Strong motions, *J. Geophys. Res.* **106,** no. B5, 8745–8766.

Guatteri, M., and P. Spudich (2000). What can strong-motion data tell us about slip-weakening fault-friction laws? *Bull. Seismol. Soc. Am.* **90,** no. 1, 98–116.

Guatteri, M., P. Spudich, and G. C. Beroza (2001). Inferring rate and state friction parameters from a rupture model of the 1995 Hyogo-ken Nanbu (Kobe) Japan earthquake, *J. Geophys. Res.* **106,** no. B11, 26,511–26,521.

Harris, R. A., and P. Segall (1987). Detection of a locked zone at depth on the Parkfield 1962, California segment of the San Andreas fault, *J. Geophys. Res.* **92,** 7945–7962.

Harris, R. A., M. Barrall, R. Archuleta, E. M. Dunham, B. T. Aagaard, J. P. Ampuero, H. Bhat, V. Cruz-Atuenza, L. A. Dalguer, P. Dawson, S. Day, B. Duan, G. Ely, Y. Kaneko, Y. Kase, N. Lapusta, Y. Liu, S. Ma, D. D. Oglesby, K. Olsen, A. Pitarka, S.-R. Song, and E. Templeton (2009). The SCEC/USGS dynamic earthquake rupture code verification exercise, *Seismol. Res. Lett.* **80,** no. 1, 119–126.

Hartzell, S., and T. H. Heaton (1983). Inversion of strong ground motion and teleseismic waveform data for the fault rupture history of the 1979 Imperial valley, California earthquake, *Bull. Seismol. Soc. Am.* **73,** no. 6, 1553–1583.

Hartzell, S., P. Liu, C. Mendoza, C. Ji, and K. Larson (2007). Stability and uncertainty of finite-fault slip inversions: Application to the 2004 Parkfield, California, earthquake, *Bull. Seismol. Soc. Am.* **97,** no. 6, 1911–1934.

Hartzell, S. H., S. Harmsen, and A. Frankel (2010). Effects of 3D random correlated velocity perturbations on predicted ground motions, *Bull. Seismol. Soc. Am.* **100,** no. 4, 1415–1426.

Heaton, T. H. (1990). Evidence for and implications of self-healing pulses of slip in earthquake rupture, *Phys. Earth Planet. In.* **64,** 1–20.

Hernandez, B., F. Cotton, and M. Campillo (1999). Contribution of radar interferometry to a two-step inversion of the kinematic process of the 1992 Landers earthquake, *J. Geophys. Res.* **104,** no. B6, 13,083–13,099.

Husseini, M. I., and M. J. Randall (1976). Rupture velocity and radiation efficiency, *Bull. Seismol. Soc. Am.* **66,** no. 4, 1173–1187.

Husseini, M. I., D. B. Jovanovich, L. M. Randall, and L. B. Freund (1975). The fracture energy of earthquakes, *J. Geophys. Res.* **43,** no. 2, 367–385.

Ide, S., and M. Takeo (1997). Determination of constitutive relations of fault slip based on seismic wave analysis, *J. Geophys. Res.* **102,** no. B12, 27,379–27,391.

Ji, C., D. Wald, and D. V. Helmberger (2002). Source description of the 1999 Hector Mine, California earthquake, Part I: Wavelet domain inversion theory and resolution analysis, *Bull. Seismol. Soc. Am.* **92,** no. 4, 1192–1207.

Ji, C., D. V. Helmberger, T.-R. A. Song, K.-F. Ma, and D. J. Wald (2001). Slip distribution and tectonic implications of the 1999 Chi-Chi, Taiwan earthquake, *Geophys. Res. Lett.* **28,** no. 23, 4379–4382.

Ji, C., D. V. Helmberger, and D. J. Wald (2004). A teleseismic study of the 2002 Denali fault, Alaska, earthquake and implications for rapid strong-motion estimation, *Earthq. Spectra* **20,** no. 3, 617–637.

Ji, C., D. V. Helmberger, D. J. Wald, and K.-F. Ma (2003). Slip history and dynamic implications of the 1999 Chi-Chi, Taiwan, earthquake, *J. Geophys. Res.* **108,** no. B9, No. 2412.

Kaneko, Y., and Y. Fialko (2011). Shallow slip deficit due to large strike-slip earthquakes in dynamic rupture simulations with elasto-plastic off-fault response, *Geophys. J. Int.* **186,** no. 3, 1389–1403.

Kaneko, Y., and N. Lapusta (2008). Variability of earthquake nucleation in continuum models of rate-and-state faults and implications for aftershock rates, *J. Geophys. Res.* **113,** no. B12312, doi: 10.1029/2007JB005154.

Kaneko, Y., and N. Lapusta (2010). Supershear transition due to a free surface in 3-D simulations of spontaneous dynamic rupture on vertical strike-slip faults, *Tectonophys* **493,** 272–284.

Kaneko, Y., N. Lapusta, and J. P. Ampuero (2008). Spectral element modeling of spontaneous earthquake rupture on rate and state faults: Effect of velocity-strengthening friction at shallow depths, *J. Geophys. Res.* **113,** no. B09317, doi: 10.1029/2007JB005553.

Knopoff, L. (1958). Energy release in earthquakes, *Geophys. J. Roy. Astron. Soc.* **1,** 44–52.

Konca, A. O., J. P. Avouac, A. Sladen, A. J. Meltzner, K. Sieh, P. Fang, Z. H. Li, J. Galetzka, J. Genrich, M. Chlieh, D. H. Natawidjaja, Y. Bock, E. J. Fielding, C. Ji, and D. V. Helmberger (2008). Partial rupture of a locked patch of the Sumatra megathrust during the 2007 earthquake sequence, *Nature* **456,** no. 7222, 631–635.

Konca, A. O., V. Hjorleifsdottir, T. R. A. Song, J. P. Avouac, D. V. Helmberger, C. Ji, K. Sieh, R. Briggs, and A. Meltzner (2007). Rupture kinematics of the 2005 M-w 8.6 Nias-Simeulue earthquake from the joint inversion of seismic and geodetic data, *Bull. Seismol. Soc. Am.* **97,** no. 1, S307–S322.

Konca, A. O., S. Leprince, J. P. Avouac, and D. Helmberger (2010). Rupture process of M_w 7.1 Duzce earthquake from joint analysis of SPOT, GPS, InSAR, strong-motion, and teleseismic data: A supershear rupture with variable rupture velocity, *Bull. Seismol. Soc. Am.* **100,** no. 1, 267–288.

Lapusta, N., and Y. Liu (2009). Three-dimensional boundary integral modeling of spontaneous earthquake sequences and aseismic slip, *J. Geophys. Res.* **114,** no. B09303, doi: 10.1029/2008JB005934.

Lapusta, N., J. R. Rice, Y. Ben-Zion, and G. Zheng (2000). Elastodynamic analysis for slow tectonic loading with spontaneous rupture episodes on faults with rate- and state-dependent friction, *J. Geophys. Res.* **105,** 23,765–23,789.

Lavallee, D., P. C. Liu, and R. J. Archuleta (2006). Stochastic model of heterogeneity in earthquake slip spatial distributions, *Geophy. J. Int.* **165,** no. 2, 622–640.

Lay, T., H. Kanamori, and L. Ruff (1982). The asperity model and the nature of large subduction zone earthquakes, *Earthq. Predic. Res.* **1,** no. 1, 3–71.

Liu, P., and R. J. Archuleta (2004). A new nonlinear finite fault inversion with three-dimensional Green's functions: Application to the 1989 Loma Prieta, California, earthquake, *J. Geophys. Res.* **109,** no. B02318, doi: 10.1029/2003JB002625.

Liu, P., S. Custodio, and R. Archuleta (2006). Kinematic inversion of the 2004 *M* 6.0 Parkfield earthquake including an approximation to site effects, *Bull. Seismol. Soc. Am.* **96,** no. 4B, S143–S158.

Liu, Y., and N. Lapusta (2008). Transition of mode II cracks from sub-Rayleigh to intersonic speeds in the presence of favorable heterogeneity, *J. Mech. Phys. Solid.* **56,** 25–50.

Madariaga, R. (1977). Implications of stress-drop models of earthquakes for the inversion of stress drop from seismic observations, *Pure Appl. Geophys.* **115,** 301–316.

Mai, P. M., D. Monelli, G. Festa, C. Francois-Holden, J. Burjanek, S. Di Carli, B. Delouis, J. Zahradnik, J. P. Ampuero, and R. Madariaga (2007). Source-inversion blindtest: Initial results and further developments, *Geophys. Res. Abstr.* **9,** no. 07351.

Monelli, D., and P. M. Mai (2008). Bayesian inference of kinematic earthquake rupture parameters through fitting of strong motion data, *Geophys. J. Int.* **173,** no. 1, 220–232.

Noda, H., N. Lapusta, and H. Kanamori (2013). Comparison of average stress drop measures for ruptures with heterogeneous stress change and implications for earthquake physics, *Geophy. J. Int.* **193,** no. 3, 1691–1712.

Oglesby, D. D., and P. M. Mai (2012). Fault geometry, rupture dynamics and ground motion from potential earthquakes on the North Anatolian Fault under the Sea of Marmara, *Geophys. J. Int.* **188,** no. 3, 1071–1087.

Olsen, K. B., R. Madariaga, and R. J. Archuleta (1997). Three-dimensional dynamic simulation of the 1992 Landers earthquake, *Science* **278,** no. 834.

Olson, A. H., and R. J. Apsel (1982). Finite faults and inverse-theory with applications to the 1979 Imperial-valley earthquake, *Bull. Seismol. Soc. Am.* **72,** no. 6, 1969–2001.

Page, M. T., S. Custodio, R. J. Archuleta, and J. M. Carlson (2009). Constraining earthquake source inversions with GPS data 1: Resolution based removal of artifacts, *J. Geophys. Res.* **114,** no. B01314, doi: 10.1029/2007JB005449.

Rice, J. R. (2006). Heating and weakening of faults during earthquake slip, *J. Geophys. Res.* **111,** no. B05311, doi: 10.1029/2005JB004006.

Rice, J. R., and Y. Ben-Zion (1996). Slip complexity in earthquake fault models, *Proc. Natl. Acad. Sci.* **93,** 3811–3818.

Ruina, A. (1983). Slip instability and state variable friction laws, *J. Geophys. Res.* **88,** no. NB12, 359–370.

Sekiguchi, H., and T. Iwata (2002). Rupture process of the 1999 Kocaeli, Turkey, earthquake estimated from strong-motion waveforms, *Bull. Seismol. Soc. Am.* **92,** no. 1, 300–311.

Sekiguchi, H., K. Irikura, and T. Iwata (2000). Fault geometry at the rupture termination of the 1995 Hyogo-ken Nanbu earthquake, *Bull. Seismol. Soc. Am.* **90,** no. 1, 117–133.

Shao, G., and C. Ji (2011). Rupture process of the 9 March, 2011 M_w 7.4 Sanriku-Oki, Japan earthquake constrained by jointly inverting teleseismic waveforms, strong motion data and GPS observations, *Geophys. Res. Lett.* **38**, no. L00G20, doi: 10.1029/2011GL049164.

Shao, G., X. Li, C. Ji, and T. Maeda (2011). Focal mechanism and slip history of the 2011 M_w 9.1 off the Pacific coast of Tohoku earthquake, constrained with teleseismic body and surface waves, *Earth Planets Space* **63,** 559–564.

Sladen, A., H. Tavera, M. Simons, J. P. Avouac, A. O. Konca, H. Perfettini, L. Audin, E. Fielding, F. Ortega, and R. Cavagnoud (2010). Source model of the 2007 M_w 8.0 Pisco, Peru earthquake: Implications for seismogenic behavior of subduction megathrusts, *J. Geophys. Res.* **115,** no. B02405, doi: 10.1029/2009JB006429.

Tinti, E., E. Fukuyama, A. Piatanesi, and M. Cocco (2005). A kinematic source-time function compatible with earthquake dynamics, *Bull. Seismol. Soc. Am.* **95,** no. 4, 1211–1223.

Trifunac, M. D., and F. E. Udwadia (1974). Parkfield, California earthquake of June 27, 1966: A three-dimensional moving dislocation, *Bull. Seismol. Soc. Am.* **64,** no. 3, 511–533.

Wald, D. J., and R. W. Graves (2001). Resolution analysis of finite fault source inversion using one- and three-dimensional Green's functions 2. Combining seismic and geodetic data, *J. Geophys. Res.* **106,** no. B5, 8767–8788.

Wald, D. J., and T. H. Heaton (1994). Spatial and temporal distribution of slip for the 1992 Landers, California, earthquake, *Bull. Seismol. Soc. Am.* **84,** no. 3, 668–691.

Wessel, P., and W. H. F. Smith (1998). New, improved version of the Generic Mapping Tools released, *EOS Trans. AGU* **79,** 579.

Xie, X., and Z. X. Yao (1989). A generalized reflection-transmission coefficient matrix method to calculate static displacement field of a dislocation source in a stratified half space, *Chin. J. Geophys.* **32,** 191–205.

Yagi, Y., and M. Kikuchi (2000). Source process of the Kocaeli, Turkey, earthquake of August 17, 1999, obtained by joint inversion of near-field data and teleseismic data, *Bull. Seismol. Soc. Am.* **27,** 1969–1972.

Zhu, L., and L. A. Rivera (2001). Computation of dynamic and static displacement from a point source in multi-layered media, *Geophys. J. Int.* **148,** no. 3, 1634–1641.

Bogazici University
Kandilli Observatory and Earthquake Research Institute
34684 Cengelkoy
Istanbul, Turkey
ozgun.konca@boun.edu.tr
(A.O.K.)

GNS Science 5010
Lower Hutt, New Zealand
y.kaneko@gns.cri.nz
(Y.K.)

Division of Engineering and Applied Science
California Institute of Technology
Pasadena, California 91125
lapusta@caltech.edu
(N.L.)

Tectonics Observatory, Division of Geological and Planetary Sciences
California Institute of Technology
1200 E. California Blvd
Pasadena, California 91125
avouac@gps.caltech.edu
(J.-P.A.)

Manuscript received 14 December 2012